Int. J. Dev. Biol. 69: 35-50 (2025)
https://doi.org/10.1387/ijdb.240147me

THE INTERNATIONAL JOURNAL OF DEVELOPMENTAL BIOLOGY
www.intjdevbiol.com

Unraveling hepatic consequences of intrauterine growth restriction and catch-up growth: insights from histological, biochemical and metabolomic analysis in rats

MUKADDES ESREFOĞLU[1], SAHABETTIN SELEK[2], FATMANUR KOKTASOGLU[2], NIHAN BAYINDIR[3], EMINE-RUMEYSA HEKIMOGLU[1], SEDA KIRMIZIKAN[1], FATMA-BEDIA KARAKAYA-CIMEN[1], HALIME DULUN-AGAC[2], MEHTAP ALIM[2], BIRSEN ELIBOL[4], OZGE PASIN[5], SOMER BEKIROGLU*[,6]

[1]Department of Histology and Embryology, Faculty of Medicine, Bezmialem Vakıf University, Istanbul, Turkey, [2]Department of Medical Biochemistry, Faculty of Medicine, Bezmialem Vakıf University, Istanbul, Turkey, [3]Department of Pathology Laboratory Techniques, Vocational High School of Health, Fenerbahce University, Istanbul, Turkey, [4]Department of Medical Biology, Istanbul Medeniyet University, Istanbul, Turkey, [5]Department of Biostatistics, Faculty of Medicine, Bezmialem Vakıf University, Istanbul, Turkey, [6]TUBITAK-Marmara Research Center, Kocaeli, Turkey

ABSTRACT Intrauterine growth restriction (IUGR) is increasingly recognized as a significant risk factor for metabolic disorders in adulthood. Employing a multi-faceted approach encompassing histopathological, immunohistochemical, biochemical, Western-blotting, and metabolomics analyses, this study aimed to elucidate potential metabolite markers of IUGR, and catch-up growth-related metabolic disturbances and the underlying metabolic pathways implicated in IUGR pathogenesis. This study cohort comprised 54 male siblings from 20 Sprague-Dawley female young rats. On the 19th day of gestation, half of the pregnant rats underwent bilateral uterine artery ligation, while the remaining half underwent a simulated surgical intervention involving solely peritoneal incisions. Blood and liver samples were collected from the pups after attaining catch-up growth at the postnatal weeks 2, 4, and 8. IUGR rats exhibited a spectrum of changes including histological abnormalities, altered apoptosis rates, oxidative stress markers, and mitochondrial energy metabolism. Metabolomic analysis revealed dysregulation in multiple metabolic pathways encompassing galactose, propanoate, glycerolipid, cysteine, methionine, and tyrosine metabolism, among others. Notably, disturbances were observed in butanoate, glutathione metabolism, valine, leucine, and isoleucine biosynthesis and degradation, citrate cycle, aminoacyl-tRNA biosynthesis, as well as glycolysis/gluconeogenesis. Our metabolomics analysis provides insights into the potential disease susceptibility of individuals born with IUGR, including obesity, diabetes, heart failure, cancer, mental retardation, kidney and liver diseases, and cataracts. These findings underscore the intricate interplay between intrauterine conditions and long-term metabolic health outcomes, highlighting the need for further investigation into preventive and therapeutic strategies aimed at mitigating the risk of metabolic diseases in individuals with a history of IUGR.

KEYWORDS: intrauterine growth restriction, liver, metabolic diseases

Introduction

Intrauterine growth restriction (IUGR), stemming from maternal, placental, fetal, or genetic factors, is defined as a rate of fetal growth that is below the expected norm for a specific child per race and gender of the fetus. An estimated 30 million newborns (23.8%) suffer from IUGR per year (Sharma *et al.,* 2016). IUGR manifests as morphological and functional changes alongside low birth weight. These changes increase the susceptibility to metabolic diseases like type-2 diabetes, obesity, hypertension, and cardiovascular diseases (Fowden *et al.,* 2006; Godfrey *et al.,* 2010; Oke *et al.,* 2021) notwithstanding achieving catch-up growth. Intrauterine programming delineates the process by which early insults during crucial developmental stages yield long-lasting morphological and functional alterations (Fowden *et al.,* 2006). The programming of adult diseases may originate from inadequate intrauterine conditions due to alterations in the development or progression of critical endocrine and metabolic pathways. This concept is defined as the 'fetal origins hypothesis' (Barker 2007).

***Address correspondence to:** Mukaddes Esrefoglu. Department of Histology and Embryology, Faculty of Medicine, Bezmialem Vakıf University, Fatih Istanbul, Turkey. E-mail: mesrefoglu@bezmialem.edu.tr | https://orcid.org/00000-0003-3380-1480

Submitted: 11 July, 2024; Accepted: 22 November, 2024; Published online: 25 March, 2025.

ISSN: Online 1696-3547, Print 0214-6282

Animal models of IUGR are invaluable tools to question the genetic, molecular and cellular events that determine fetal growth and development. The findings obtained from animal models bear similarities to those recorded in humans born small for gestational age and are noteworthy due to established correlation between poor fetal growth and emergence of adult diseases (Vuguin 2007). Bilateral uterine artery ligation is one of the various interventions used for creating inadequate intrauterine condition to induce growth retardation (Wigglesworth 1964). Caloric restriction, low protein diet, iron deficiency, utero-placental embolization, genetic interventions are among the other IUGR methods (Vuguin 2007). Similar to humans, fetal rats in this model suffer from transient hypoglycemia, hypoxia, and acidosis and demonstrate the long-term effects of the altered intrauterine milieu (Simmons *et al.,* 1992; Ogata *et al*.1986).

Fetal tissues are extremely vulnerable to internal or external stressors. Several genes from the mother, the fetus, and the placenta are implicated in IUGR (Sharma *et al.,* 2017). Apoptosis, autophagy, endoplasmic reticulum (ER) stress, oxidative stress, inflammation, and mitochondrial dysfunction are suggested to contribute to the metabolic alterations observed in IUGR (Oke *et al.,* 2021; Gurugubelli Krishna *et al.,* 2018; Rashid *et al.,* 2018). Due to cellular stress and programmed cell death induced by genetic or epigenetic factors, individuals born with IUGR are predisposed to metabolic disorders. The liver, pancreas, adipose tissue, and muscle tissue exhibit high susceptibility to oxidative stress and mitochondrial dysfunction in individuals with a history of IUGR (Oke *et al.,* 2021; Pendleton *et al.,* 2021). Emerging evidence suggests the liver may represent one of the candidate organs undergoing structural, functional, and epigenetic changes in response to unfavorable intrauterine conditions (Cianfarani *et al.,* 2012). Hepatic as well as pancreatic oxidative damage potentially contribute to the development of insulin resistance and diabetes (Oke *et al.,* 2021).

Limited studies investigating the IUGR-induced changes in the hepatic metabolomics and related long-term metabolic effects have been performed (Liu *et al.,* 2022, Ponsuksili *et al.,* 2022). Currently data on the hepatic involvement in the developmental origins of metabolic diseases are limited leaving numerous unanswered questions regarding the primary and secondary pathways implicated. Although some molecular pathways have been hypothesized on the emergence of diseases linked to IUGR, significant gaps in understanding persist. Through an examination of liver programming, which raises metabolic risk in IUGR patients even when catch-up growth is present, this research attempts to shed light on the molecular mechanisms underlying this condition. With a wide range of techniques applied, such as immunohistochemistry, biochemistry, Western blotting, and metabolomics analyses, our goals are to identify important metabolic pathways implicated in the pathophysiology of IUGR, provide insights into diseases presumed to be linked to IUGR, and clarify putative metabolite markers of IUGR- related metabolic disorders. We anticipate that the results of this study will provide a solid platform for future research into the mechanisms behind IUGR-related disorders.

Results

Body weights

The mean body weights of the pups from the IUGR and Sham groups were similar in the 2nd week. However, the mean body weights of the pups from IUGR in the 4th ($p<0.05$) and 8th weeks were higher than those of the Sham group in the corresponding weeks. Notably, the catch-up growth was evident as early as the 2nd postnatal week (Fig. 1).

Histopathological analyses

The histopathological analyses revealed some differences between the IUGR and Sham groups. In the sections from the 2-week-old rats in the Sham group, classical hepatic lobules were not distinctly discernible, with central veins and portal areas appearing randomly arranged compared to healthy adult livers. Moreover, the portal areas lacked conspicuous connective tissue, hindering the recognition (Fig. 2 A,B). Evidence of ongoing hemopoiesis was observed, characterized by dispersed hematopoietic cell groups (Fig. 2A). Similarly, sections from 2-week-old rats in the IUGR group exhibited indistinct classical hepatic lobules with some areas devoid of central veins and the elements of the portal triad including portal vein, portal artery, and bile duct. These areas were occupied by rows of hepatocytes (Fig. 2C). Prominent vacuolization and perinuclear edema were detected in these sections. Additionally, larger hematopoietic cell groups were dispersed compared to the Sham group (Fig. 2D).

In the sections from 4-week-old rats in the Sham group, liver histology exhibited greater similarity to that of healthy adult liver. Classical hepatic lobules were discernible, and the connective tissue elements of portal areas, although not abundant, were detectable (Figs. 3 A,B). Hemopoiesis was still ongoing within small hematopoietic cell groups (Fig. 3A). Similarly, sections from 4-week-old rats in the IUGR group displayed discernible classical hepatic lobules (Figs. 3 C,D), although some areas were still solely occupied by rows of hepatocytes without central veins or portal spaces. Notably, perinuclear edema was obvious in the cytoplasm of the hepatocytes located in these areas (Fig. 3C). Hemopoiesis persisted, with larger hematopoietic cell groups compared to Sham (Fig. 3D).

In the sections of 8-week-old rats in the Sham group, liver histology closely resembled that of a healthy adult liver. Classical hepatic lobules were easily identifiable, and the connective tissue connective tissue of portal areas was detectable (Figs. 4 A,B). Similarly, sections from 8-week-old rats in the IUGR group displayed predictable classical hepatic lobules, yet some areas

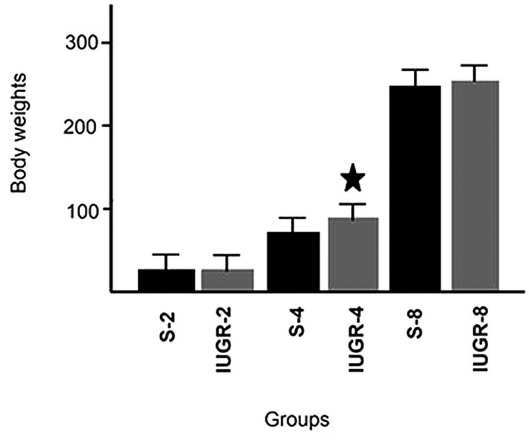

Fig. 1. Mean body weights of the groups at the end of the 2nd, 4th and 8th weeks. * $p<0.05$ vs Sham group.

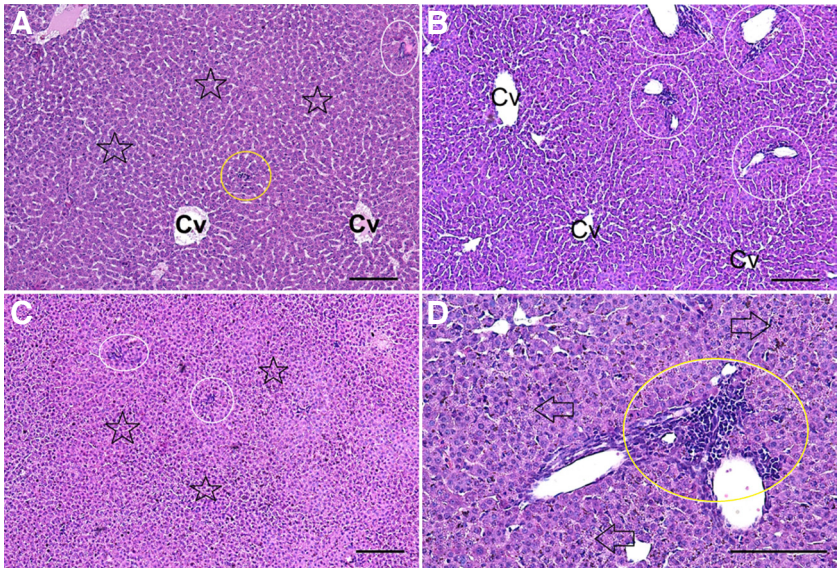

Fig. 2. Liver histology of 2-week-old groups. Sections obtained from 2-week-old Sham group **(A,B)** and 2-week-old IUGR group **(C,D). (A,B)** Classical hepatic lobule organization is absent (stars). Central veins (CV) and hardly recognized portal areas (white circle) are organized randomly. Small hematopoietic cell groups are observed (yellow circle). **(C,D)** Classical hepatic lobules are not obvious (stars). Portal areas generally are barely recognizable since connective tissue is absent or very thin (C). Hematopoietic cell groups at the portal area are circled (yellow circle) (D). Hematoxylin and eosin staining technique. Scale bars, 100 µm.

remained occupied by only rows of hepatocytes with no sign of central vein or portal elements (Figs. 4 C,D). The distribution of central veins and the portal areas appeared more random than typical lobule organization. Perinuclear edema was rarely detected (Fig. 4D).

The mean numbers of central veins and portal areas were non-uniform between the Sham and IUGR groups indicating disruption of classical hepatic lobules. IUGR altered the mean numbers of central veins and portal areas. Specifically, the mean number of the central veins of the 4- and 8-week- old IUGR group was higher than that of the 4- and 8-week-old Sham group ($p<0.001$, $p<0.05$; respectively). Additionally, the mean number of portal areas in the 2-week-old IUGR group was higher than that in the 2-week-old Sham group ($p<0.001$) (Fig. 5).

Immunohistochemical analyses

The distribution of Ki-67 + and caspase-8 + cells appeared similar across all developmental weeks in both the Sham and IUGR groups. However, statistical analysis revealed significant differences in cell counts between corresponding Sham and IUGR groups. Ki-67 + cells were distributed throughout the liver parenchyma as well as the stroma in all groups. Specifically, the mean number of Ki-67 + cells in the 8-week-old rats from the IUGR group was significantly higher than that of the Sham group ($p<0.05$). Caspase cells were also detected in the liver parenchyma as well as the stroma in all groups. Additionally, the mean number of caspase-8 + cells in the IUGR group was higher than that in the Sham group at 2, 4, and 8th weeks of age ($p<0.05$, $p<0.05$, $p<0.001$; respectively).

Western blotting analyses

The tissue RIP3/GAPDH level in the 2-week-old IUGR group was found to be lower than that in the 2-week-old Sham group ($p<0.005$). Conversely, the tissue NF-kB level of the 2- and 8-week-old IUGR groups was lower than the corresponding Sham groups ($p<0.005$, $p<0.001$; respectively). However, the NF-kB level in

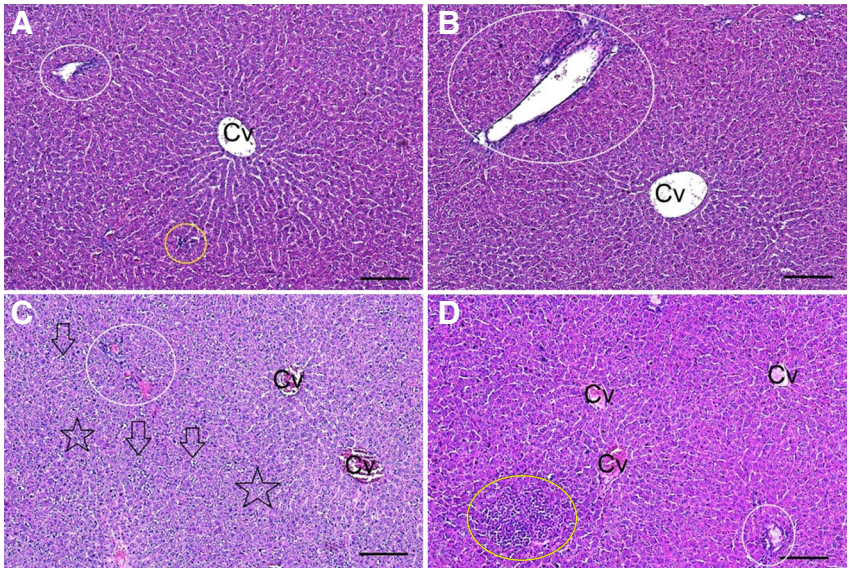

Fig. 3. Liver histology of 4-week-old groups. Sections obtained from 4-week-old Sham group **(A,B)** and of 4-week-old IUGR group **(C,D)**. **(A,B)** Classical hepatic lobules containing central vein (CV) at the center and portal area (white circle) at the periphery are predictable. Small hematopoietic cell groups are observed (yellow circles). **(C,D)** Classical lobule organization is not fully developed. Although classical hepatic lobules containing a central vein (CV) at the center and portal area (white circle) at the periphery are predictable, some areas are occupied by only randomly distributed hepatocytes (stars). Especially in the cytoplasm of the hepatocytes located in those areas, perinuclear edema is obvious (arrows). Larger hematopoietic cell groups than those of the Sham group are observed (yellow circle). Hematoxylin and eosin staining technique. Scale bars, 100 µm.

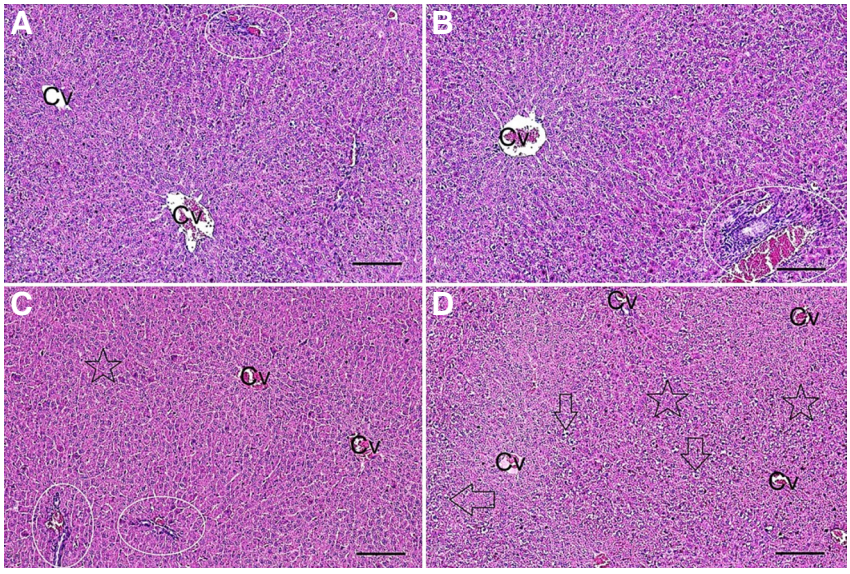

Fig. 4. Liver histology of 8-week-old groups. Sections obtained from 8-week-old Sham group **(A,B)** and the 8-week-old IUGR group **(C,D). (A,B)** Classical hepatic lobules containing a central vein (CV) at the center and portal area (white circle) at the periphery are obvious. **(C,D)** Classical hepatic lobules are not well organized. Central veins are generally randomly distributed. Some areas are occupied by only hepatocyte rows but not central vein or portal elements (stars). Especially in the cytoplasm of the hepatocytes located in those areas, perinuclear edema is obvious (arrows). Hematoxylin and eosin staining technique. Scale bars, 100 µm.

the 4-week-old IUGR group was higher than that in the 4-week-old Sham group (p<0.05). These findings suggest alterations in necroptosis and inflammation patterns between the equivalent weeks of the Sham and IUGR groups, underscoring potential differences in underlying molecular mechanisms associated with IUGR (Fig. 6).

Biochemical analyses of the serum samples

Biochemical analysis of the serum samples from 2-week-old rats were precluded due to insufficient sample volume. However, significant differences were observed in the levels of IDH and MDH between Sham and IUGR groups at 4 and 8 weeks of age. Specifically, the mean IDH level in the 4-week-old IUGR group was higher than that in the 4-week-old Sham group (p<0.05). Conversely, the mean IDH level in the 8-week-old IUGR group was lower than that in the 8-week-old Sham group (p<0.05). Additionally, the mean MDH level in the 8-week-old IUGR group was lower than that in the 8-week-old Sham group (p<0.05)Biochemical analyses of the tissue samples

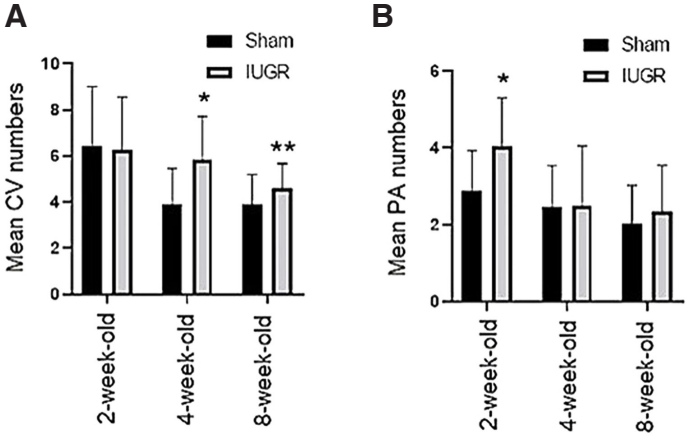

Fig. 5. Mean numbers of central veins (CV) and portal areas of the groups. * p<0.001, ** p<0.05.

Significant differences were observed between IUGR and Sham groups regarding mean tissue levels of TOS, TAS, TThiol, NThiol, glutamate dehydrogenase, glucose-6-phosphate dehydrogenase, NAD-isocitrate dehydrogenase (NAD-IDH), NADP-isocitrate dehydrogenase (NADP-IDH), fumarase, Zn, and Cu.

Tissue TOS and TAS levels

No significant changes in terms of the mean TOS levels between the IUGR and Sham groups were detected. The mean TAS level of the 2-week-old IUGR group was lower than that of the 2-week-old Sham group (p<0.05), however, the mean TAS levels of the 4- and 8-week- old IUGR groups were not significantly different from those of the corresponding Sham groups.Tissue TThiol and NThiol levels

The mean TThiol level in the 2-week-old IUGR group was found to be lower than that of the 2-week-old Sham group (p<0.05), while the level in the 4-week-old IUGR group was higher than that in the 4-week-old Sham group (p<0.05). The mean NThiol level in the 2- week-old IUGR group was lower than that in the 2-week-old Sham group (p<0.005), whereas the level in the 8-week-old IUGR group was higher than that in the 8-week-old Sham group (p<0.05).Tissue glutamate dehydrogenase levels

The mean GDH level in the 4-week-old IUGR group was higher than that in the 4-week-old Sham group (p<0.05).Tissue glucose-6-phosphate dehydrogenase levels

The mean G-6-P dehydrogenase level in the 2- week-old IUGR group was lower than that in the 2-week-old Sham group (p<0.05), while the level in the 4-week-old IUGR group was higher than that in the 4-week-old Sham group (p<0.05).Tissue isocitrate dehydrogenase levels

The mean NADP-IDH level in the 2-week-old IUGR group was lower than that in the 2-week-old Sham group, while the level in the 4-week-old IUGR group was higher than that in the 4-week-old Sham group (p<0.05). Additionally, the mean NAD-IDH level in the 8-week-old IUGR group was higher than that in the 8-week-old Sham group (p<0.05).Tissue fumarase levels

The mean fumarase level in the 2-week-old IUGR group was lower than that in the 2-week-old Sham group (p<0.001), while the

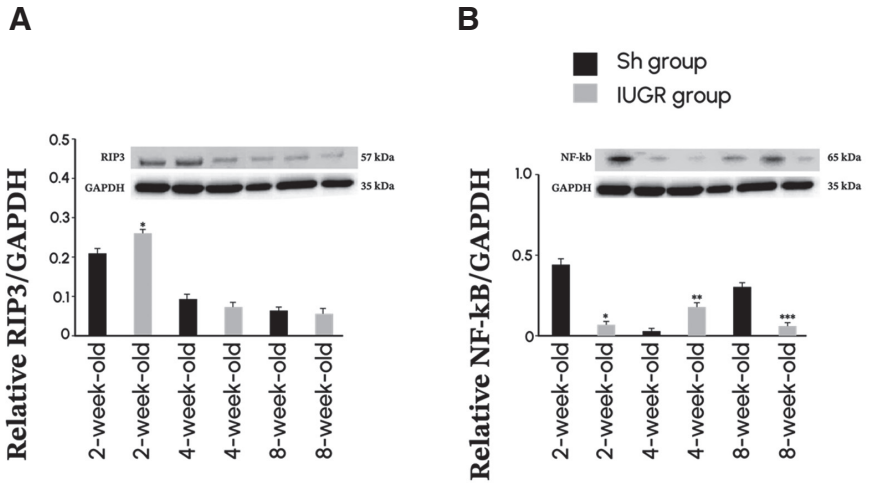

Fig. 6. Tissue RIP3/GAPDH and NF-kB levels of the groups. * p<0.005, ** p<0.05, *** p<0.001.

levels in the 4- and 8-week-old IUGR groups were higher those in the corresponding Sham groups (p<0.05).

Tissue zinc and copper levels

The mean zinc level in the 2-week-old IUGR group was higher than that in the 2-week-old Sham group (p=0.001), whereas the copper level in the 2-week-old IUGR group was lower than that in the 2-week-old Sham group (p<0.05). The mean zinc level in the 4-week- old IUGR group was lower than that in the corresponding Sham group (p<0.005). Additionally, the mean zinc and copper levels in the 8-week-old IUGR group were higher than that in the 8-week-old Sham group (p<0.05, p<0.005; respectively).

Metabolomics analyses

Upon examining the results of the metabolomics in the 2-week-old IUGR and Sham groups, significant alterations were uncovered. Illustrated in the volcano plot graph (Fig. 7A), the IUGR group exhibited elevated levels of succinate, acetoacetate, isoleucine, cytidine, and formate, while displaying decreased levels of citrate, isocitrate, glucose, glucose-1-phosphate, maltose, and homocysteine to the Sham group. Utilizing Principal Component Analysis (PCA), which is adept at discerning patterns within high-dimensional data, the complexity of the data was effectively mitigated. The PCA score plots derived from NMR spectroscopy -analyzed tissue samples convincingly demonstrated group segregation and intra-group data clustering, accounting for approximately 63.15% of the variables. As depicted in Fig. 7B, the first principal component (PC1) accounted for 47.3% of the variance, while the second principal component (PC2) accounted for 15.8% of the variance. Further insights were gleaned through orthogonal partial least square data analysis (OPLS-DA), a method facilitating detailed examination of multivariate data. The OPLS-DA graph (Fig. 7C) affirmed successful differentiation between the IUGR and Sham groups.

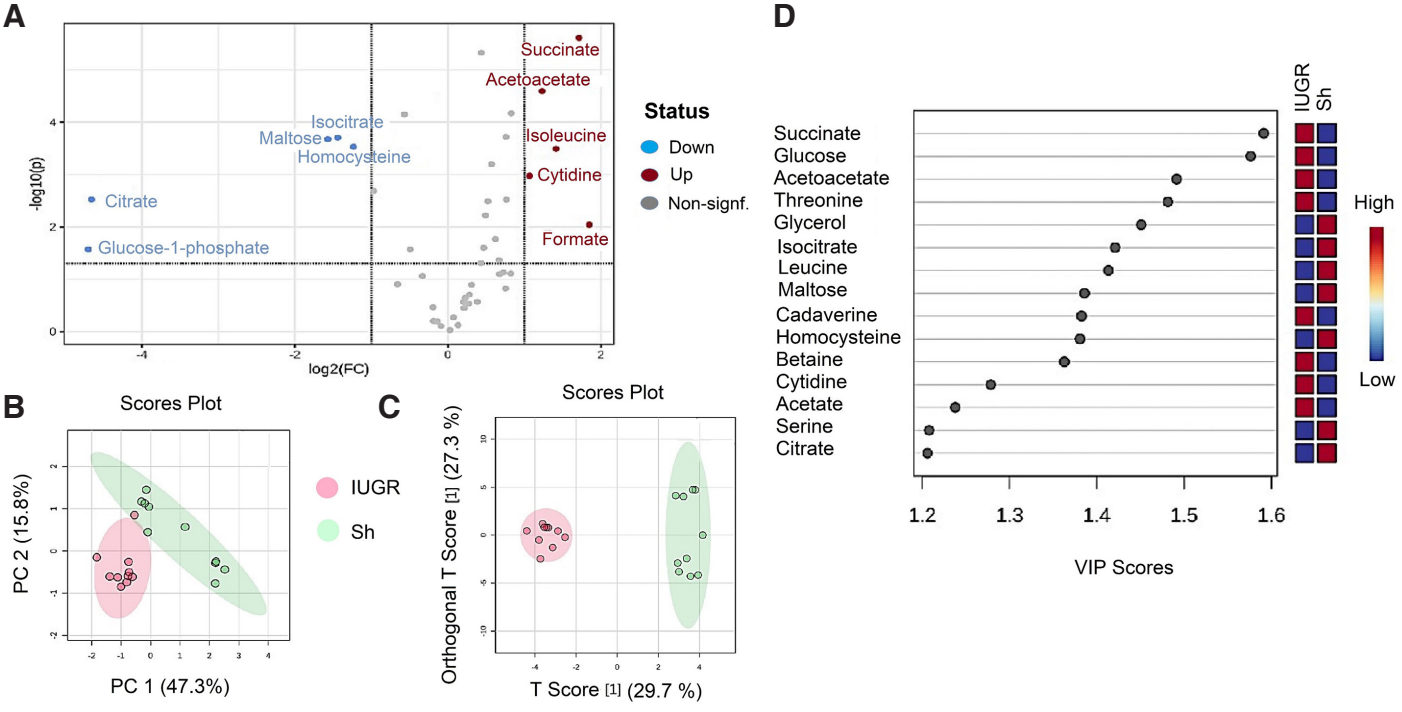

Fig. 7. The metabolomics results of the 2-week-old Sham and IUGR group. (A) Volcano plot graph shows elevated and depleted metabolomics in the IUGR group versus the Sham group. **(B)** PCA 2D score-plot of NMR dataset. The IUGR group is depicted as red, and the Sham group is represented by green data points. Additionally, T2 Hotelling's ellipses were employed to define a 95% confidence level for the IUGR group, further highlighting its separation from the Sham group. **(C)** The OPLS-DA graph shows a separation between the IUGR and Sham groups. **(D)** The OPLS-DA graph shows the metabolites that exhibited the greatest contribution to the observed separation.

Additionally, the VIP score graph (Fig. 7D) showcased metabolites such as succinate, glucose, and acetoacetate as pivotal in distinguishing between groups. These findings underscore the utility of metabolomics in unraveling metabolic distinctions associated with IUGR.

Upon analyzing tissue samples extracted from 4-week-old rat livers, notable disparities emerged in the levels of acetoacetate, ethanol, pyruvate, cadaverine, and ethanolamine, which were found to be significantly elevated in the IUGR group compared to the Sham group. The volcano plot graph depicting statistically significant differential metabolites and fold change is illustrated in Fig. 8A. While a distinct separation was not readily apparent through PCA (Fig. 8B), the application of OPLS-DA proved instrumental in delineating the IUGR and Sham groups based on their metabolic profiles (Fig. 5C). OPLS-DA results depicted in Fig. 8C underscore the efficacy of this analysis in discerning the metabolic distinctions between the two groups. Fig. 8D highlights the metabolites most closely associated with this discrimination.

Upon analyzing the NMR spectroscopy dataset obtained from 8-week-old rats, a distinct group of metabolites including acetoacetate, niacinamide, valine, phenylalanine, glutamate, cytidine, glucose, uracil, cadaverine, isoleucine, 1-methyhistidine, methionine, glucuronate, glycine, and fumarate exhibited an exclusive increase in the IUGR group (Fig. 9A). Despite the lack of a clear differentiation between the groups through PCA (Fig. 9B), successful distinction was achieved through OPLS-DA (Fig. 9C). The OPLS-DA illustrated a discernible separation, indicative of distinct metabolic profiles between the IUGR and Sham groups. Further examination revealed the metabolites contributing most significantly to this observed separation (Fig. 9D), underscoring their pivotal role in discriminating between the IUGR and Sham groups. These findings highlight the efficacy of OPLS-DA in uncovering metabolic distinctions associated with IUGR and identifying potential biomarkers warranting further investigation.

Meta-analyses

To conduct the meta-analysis, all samples were stratified based on their respective groups: IUGR and Sh. The meta-analysis involved samples from animals at three different weeks of age. Upon meta-analysis of the values of the 2-week-old group, 25 significantly different metabolites were identified. In both the 4-week-old and 8-week-old groups, two metabolites exhibited significant differences (Fig. 10A). Of these metabolites, a total of 25 metabolites were detected specifically in the 2-week-old group, with 23 being unique being unique to this age group. The identified metabolites in the 2-week-old group included 3-amino isobutyrate, acetate, acetoacetate, aspartate, betaine, cadaverine, citrate, cytidine, ethanolamine, formate, glucose, glucose-1-phosphate, glutamate, glycine, homocysteine, isocitrate, maltose, phenylalanine, proline, pyruvate, succinate, threonine, tyrosine, uracil, and valine. Among these metabolites, acetoacetate emerged as the most distinct potential metabolite for selecting IUGR independently of the animal's age. Its discriminatory ability remained consistent across different age groups, indicating its potential as a reliable marker for distinguishing IUGR from non-IUGR conditions. The expression patterns of acetoacetate and valine comparing all 3 groups are depicted in Fig. 10B.

Following the comprehensive analysis of merged data from three different age groups, a volcano plot graph depicting

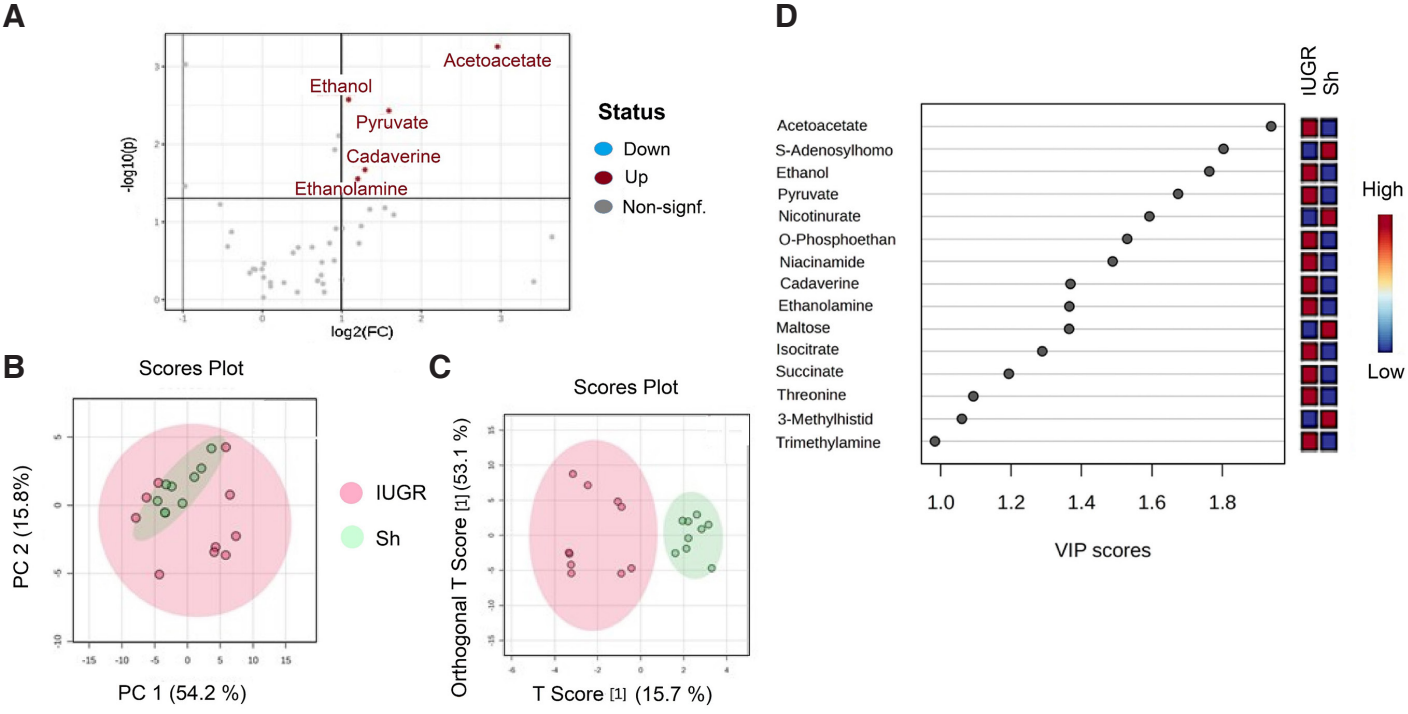

Fig. 8. The metabolomics results of the 4-week-old Sham and IUGR group. (A) Volcano plot graph shows elevated metabolomics in the IUGR group versus the Sham group. **(B)** PCA 2D score-plot of the NMR dataset shows that the metabolite profiles are similar. **(C)** The OPLS-DA graph shows a separation between the IUGR and Sham groups. **(D.** The OPLS-DA graph shows the metabolites that made the most substantial contributions to the observed separation.

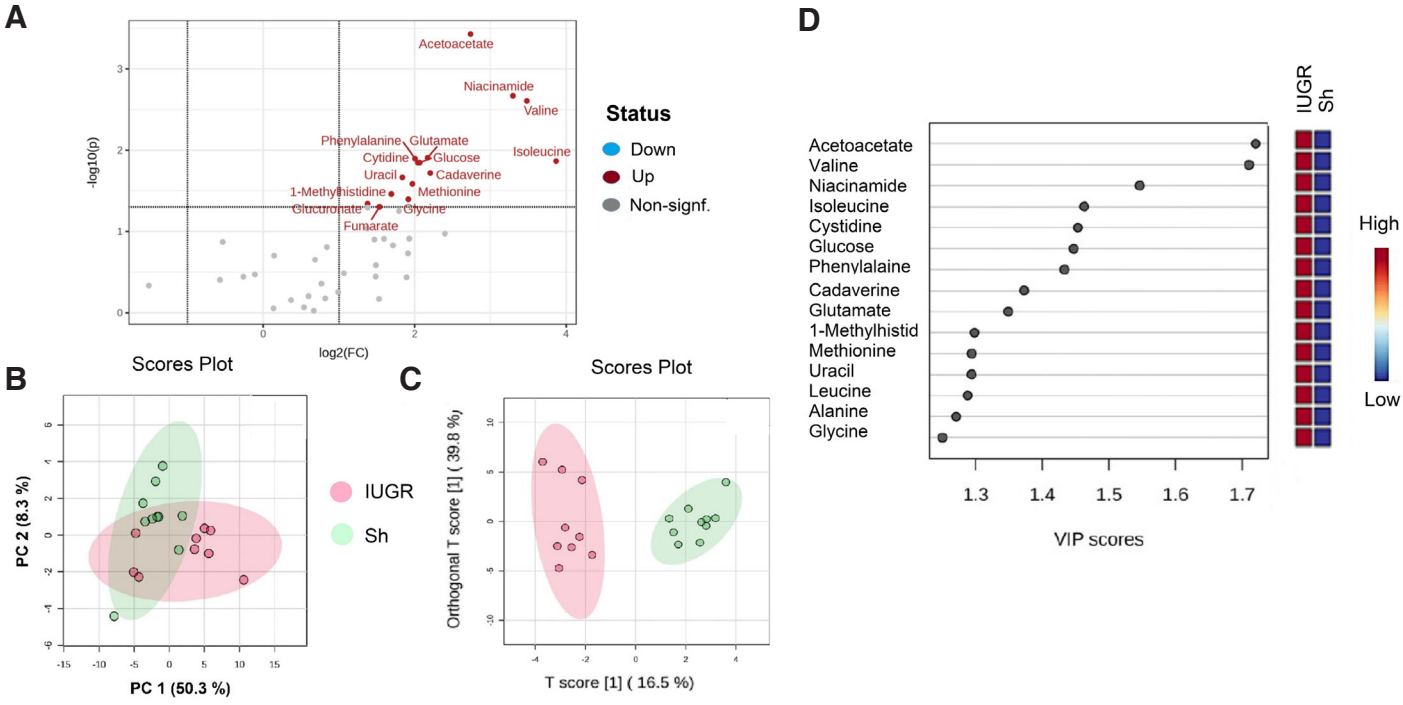

Fig. 9. The metabolomics results of the 8-week-old Sham and IUGR group. (A) Volcano plot graph shows elevated metabolomics in the IUGR group versus the Sham group. **(B)** PCA 2D score-plot of the NMR dataset represents the principal components of the analysis. **(C)** The OPLS-DA graph shows a separation between the IUGR and Sham groups. **(D)** The OPLS-DA graph shows the metabolites that made the most substantial contributions to the observed separation.

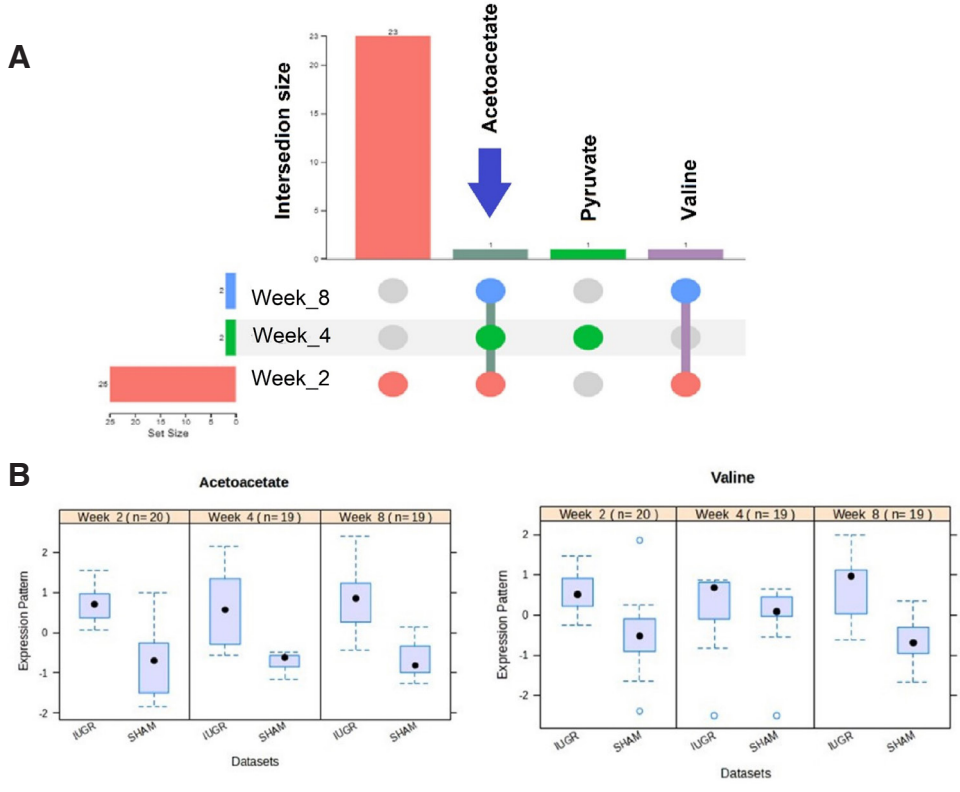

Fig. 10. Results of a meta-analysis of the values of the metabolites of all groups. (A) Distinctive metabolites identified for discrimination between IUGR and Sham groups across all ages. The blue arrow indicates there was one metabolite to distinct Sham or IUGR group among all ages. **(B)** Expression patterns of two significant metabolites according to meta-analysis.

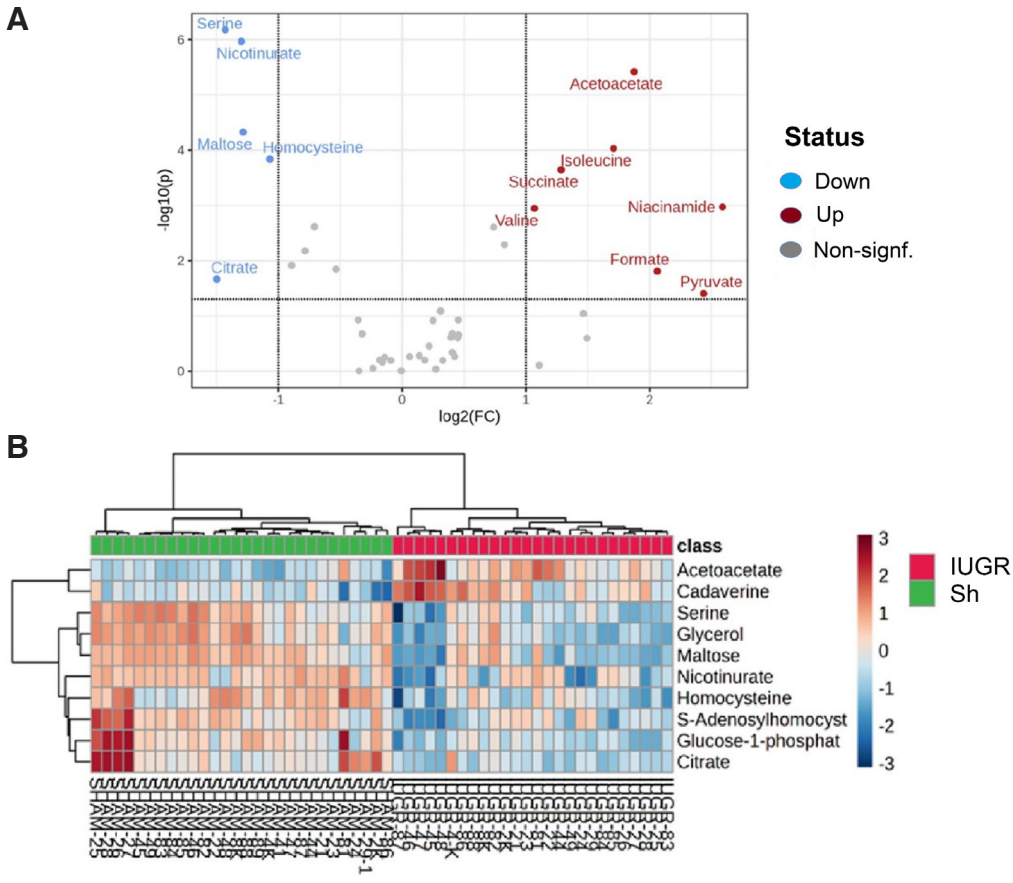

Fig. 11. Differential metabolite levels of the Sham and IUGR groups. (A) Volcano plot graph of all samples separated according to Sham and IUGR groups. **(B)** Metabolite abundance Heatmap of IUGR and Sham groups.

differential metabolite levels between the IUGR group and the Sham group was generated (Fig. 11A). Notably, acetoacetate, isoleucine, succinate, valine, niacinamide, formate, and pyruvate exhibited increased levels in the IUGR groups compared to the Sham groups. Conversely, serine, nicotinurate, maltose, homocysteine, and citrate levels were decreased in the IUGR groups versus the Sham groups. The heatmap presented in Fig. 11B illustrates the relative abundance of metabolites across the IUGR and Sham groups. Each row represents a metabolite, while each column corresponds to a sample. The color gradient in the heatmap reflects the magnitude of the variable's abundance with red shades indicating higher values and blue shades indicating lower values. Although PCA did not yield a clear distinction between the groups (Fig. 12A), a discernible differentiation was successfully achieved through OPLS-DA (Fig. 12B). Further analysis pinpointed the metabolites contributing most significantly to the observed separation (Fig. 12C).

Enrichment and pathway analyses

With the comprehensive dataset analysis, data of all samples were evaluated separately. Fig. 13A presents the top 25 biological processes that were found to be most significantly affected in the enrichment analysis obtained with merged data. This analysis employs statistical methods to assess the relationship between metabolites within the data set and relevant pathways. The identified biological processes represent key functional categories that exhibit significant associations with the metabolite data. The inclusion of these processes provides valuable insights into the potential biological mechanisms underlying the observed metabolic changes. Enrichment analysis revealed ketone body metabolism, butyrate metabolism, and methionine metabolism as the most influenced pathways. The most affected pathways and related metabolites revealed by the pathway analysis are depicted in Figs. 13A and 13B.

The visualization of results and enrichment analysis for the subgroups is presented in Fig. 14. Fig. 14A highlights the most affected pathways including the oxidation of branched-chain fatty acids, phytanic acid peroxisomal oxidation, and valine leucine and isoleucine degradation in the 2-week-old group. These pathways demonstrate significant associations with the metabolite profiles observed in this group, indicating notable alterations in these metabolic pathways during early development. In the 4- week-old group betaine metabolism, tryptophan metabolism, and ubiquinone metabolism were found to be the most affected pathways (Fig. 14B). In the 8-week-old group, propanoate metabolism, valine, leucine, and isoleucine degradation, and ketone body metabolism were detected as the most influenced pathways (Fig. 14C). These pathway perturbations highlight the distinctive metabolic signatures present in the aged 8-week group. Overall, the visualization of these results offers valuable insights into the specific pathway dysregulations within each age group,

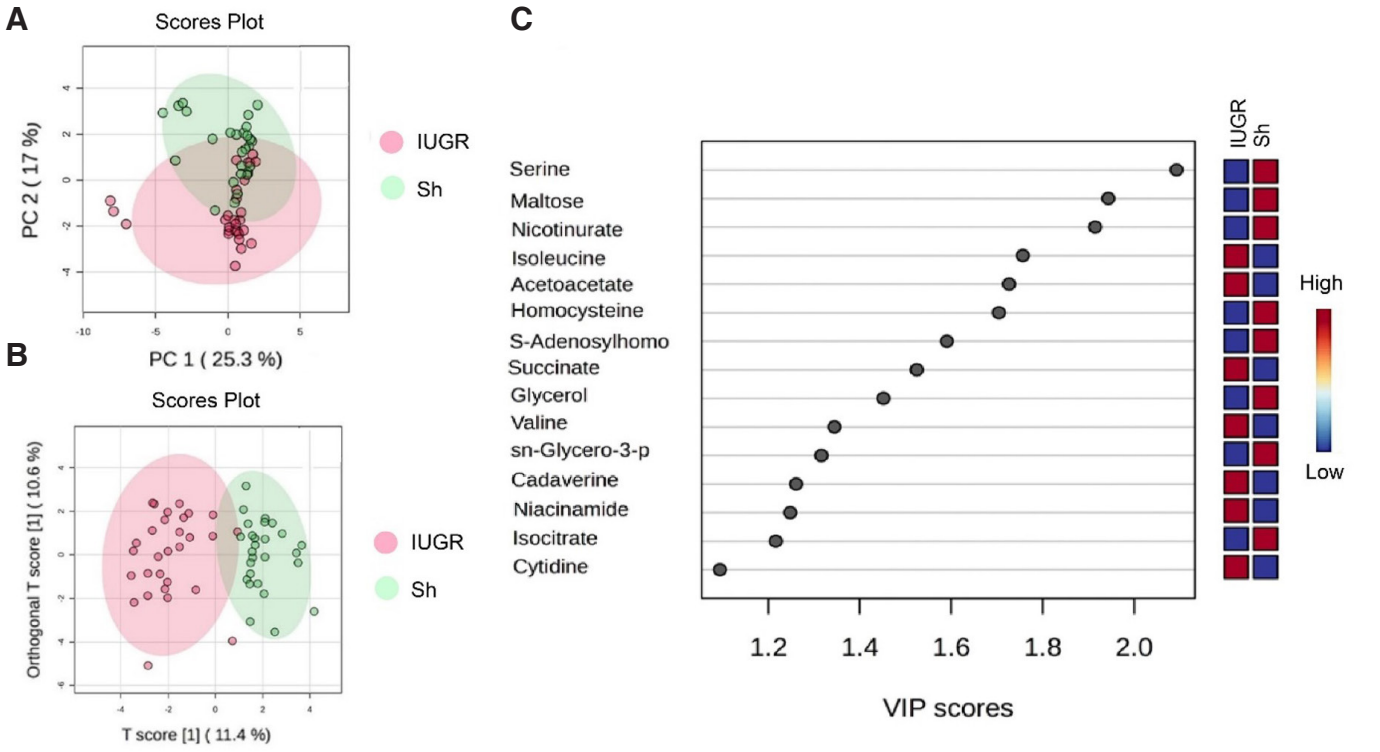

Fig. 12. Further analysis results on distinction between groups. (A) PCA analysis visualization of all samples. No distinctive pattern in metabolites is observed. **(B)** The OPLS-DA graph was obtained with a dataset of all samples. A separation between the IUGR and Sham groups was observed. **(C)** The metabolites that made the most substantial contributions to the observed separation are listed.

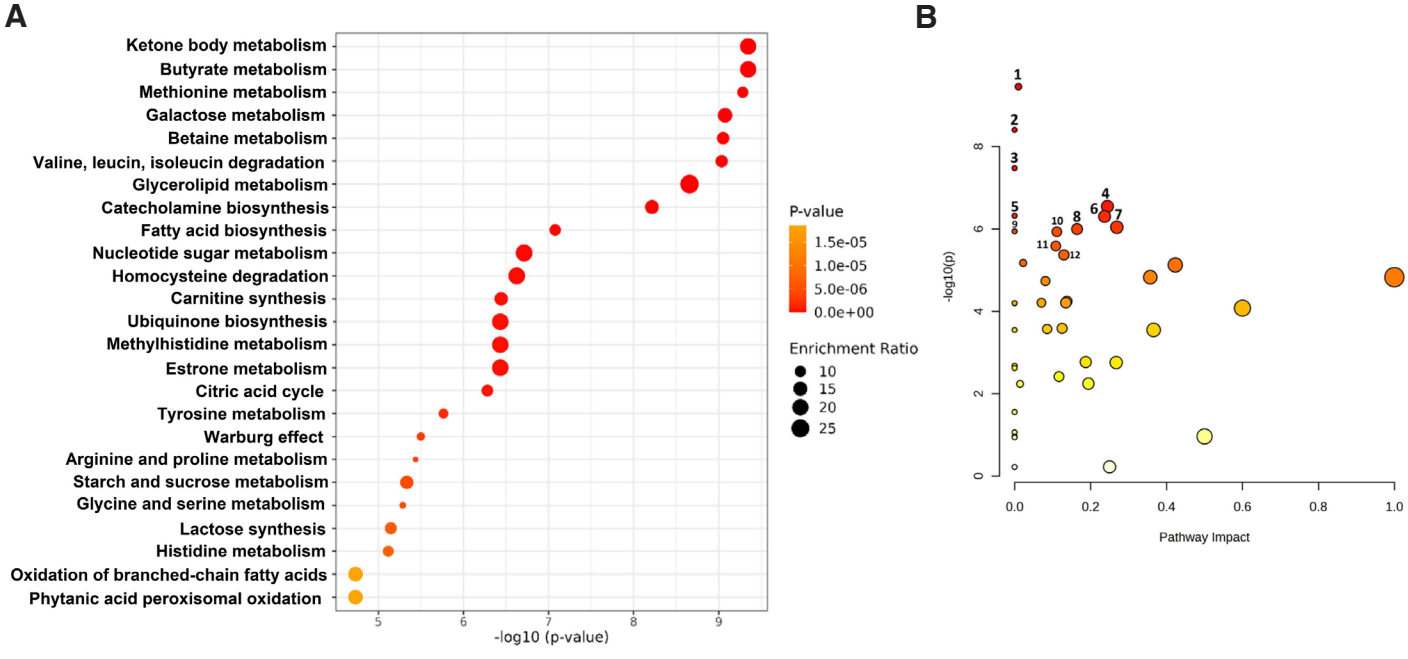

Fig. 13. The most significantly affected biological processes. (A) Enrichment analysis conducted with the merged dataset. The top 25 biological processes that were found to be most significantly affected are listed. **(B)** Visualization of pathway analysis conducted with merged data. The numbers of the most influenced pathways are shown in Figure as follows: 1. Galactose metabolism, 2. Valine, leucine and isoleucine degradation, 3. Valine, leucine, and isoleucine biosynthesis, 4. Citrate cycle (TCA cycle, 5. Propanoate metabolism, 6. Glycerolipid metabolism, 7. Cysteine and methionine metabolism, 8. Tyrosine metabolism, 9. Aminoacyl-tRNA biosynthesis, 10. Butanoate metabolism, 11. Glutathione metabolism, 12. Glycolysis / Gluconeogenesis.

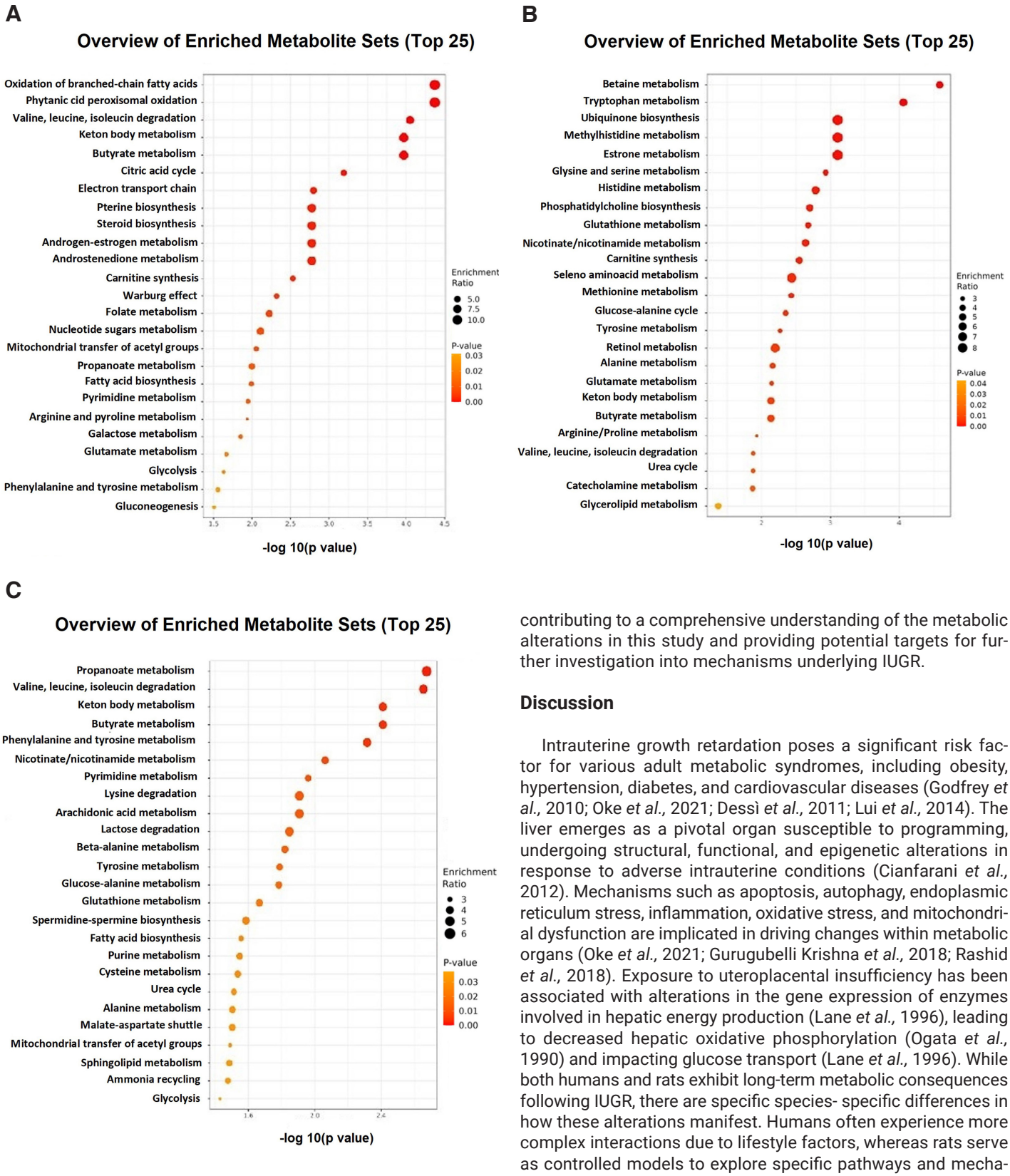

Fig. 14. Enrichment analysis of the groups. Identification of dysregulated pathways in IUGR groups for aged **(A)** 2 weeks, **(B)** 4 weeks, **(C)** 8 weeks.

contributing to a comprehensive understanding of the metabolic alterations in this study and providing potential targets for further investigation into mechanisms underlying IUGR.

Discussion

Intrauterine growth retardation poses a significant risk factor for various adult metabolic syndromes, including obesity, hypertension, diabetes, and cardiovascular diseases (Godfrey *et al.*, 2010; Oke *et al.*, 2021; Dessì *et al.*, 2011; Lui *et al.*, 2014). The liver emerges as a pivotal organ susceptible to programming, undergoing structural, functional, and epigenetic alterations in response to adverse intrauterine conditions (Cianfarani *et al.*, 2012). Mechanisms such as apoptosis, autophagy, endoplasmic reticulum stress, inflammation, oxidative stress, and mitochondrial dysfunction are implicated in driving changes within metabolic organs (Oke *et al.*, 2021; Gurugubelli Krishna *et al.*, 2018; Rashid *et al.*, 2018). Exposure to uteroplacental insufficiency has been associated with alterations in the gene expression of enzymes involved in hepatic energy production (Lane *et al.*, 1996), leading to decreased hepatic oxidative phosphorylation (Ogata *et al.*, 1990) and impacting glucose transport (Lane *et al.*, 1996). While both humans and rats exhibit long-term metabolic consequences following IUGR, there are specific species- specific differences in how these alterations manifest. Humans often experience more complex interactions due to lifestyle factors, whereas rats serve as controlled models to explore specific pathways and mechanisms. However, the similarities in insulin resistance, obesity, lipid metabolism, mitochondrial dysfunction, and epigenetic

changes between both species make rats valuable models for studying the underlying mechanisms of IUGR-related metabolic dysfunction in humans.

According to the histopathological findings of our study, it is evident that IUGR significantly impairs liver development. The classical organization of the hepatic lobule was disrupted, accompanied by notable vacuolization and perinuclear edema. These observations align with previous studies by Zhang *et al.,*Zhang *et al.,* 2018; Zhang *et al.,* 2020) which report similar IUGR-induced vacuolation and parenchymal disorganization. Furthermore, our study revealed a sustained increase in caspase-8 + cell numbers, persisting even in the postnatal 8 weeks ($p<0.005$). This finding corroborates with prior research indicating elevated hepatocyte apoptosis rates in IUGR conditions (Lui *et al.,* 2014; Zhang *et al.,* 2018; Zhang *et al.,* 2020; Zhang *et al.,* 2021). Moreover, the increased tissue RIP3 level in the 2-week- old IUGR group ($p<0.005$) suggests the involvement of necroptosis, at least during the early postnatal period in rats affected by IUGR. This implies a broader spectrum of cell death mechanisms at play in response to IUGR-induced stress. The dysregulation observed in tissue NF-kB levels, a central mediator in inflammation, stress response, cell differentiation, proliferation, and cell death, further underscores abnormalities in hepatocyte metabolism induced by IUGR. Consistent with our findings, Zhang *et al.,* (Zhang *et al.,* 2020) reported elevated hepatic NF-Kb p65 levels along with apoptosis antigen-1, Bax, cytochrome-c, and TNF-α levels in the liver of IUGR lambs.

Studies have consistently reported increased oxidative stress in both the serum and the livers of newborns affected by IUGR (Zhang *et al.,* 2018; Zhang *et al.,* 2021; Saker *et al.,* 2008; Wang *et al.,* 2022). This heightened hepatic oxidative stress is often attributed to an imbalance between the accumulation of free radicals and the production of antioxidant enzymes (Zhang *et al.,* 2020; Wang *et al.,* 2008). Notably, the levels of antioxidant enzymes are lower in IUGR newborns compared to their healthy counterparts (Smith *et al.,* 1993; Sullivan *et al.,* 1988). Oxidative stress, a pivotal factor in the pathogenesis of IUGR, is closely linked to uteroplacental insufficiency, which contributes to early liver injury (Biri *et al.,* 2007). However, in our study, we did not find significant evidence of increased oxidative stress in IUGR groups except for a decrease in TAS level in the 2-week-old IUGR group ($p<0.05$). We observed reductions in TThiol and NThiol levels ($p<0.05$, $p<0.005$; respectively) which are organic compounds essential for protection against oxidative damage. Interestingly, by the 8th week, the TThiol level had normalized, while the NThiol level had increased instead ($p<0.05$). These findings suggest a potential restoration of the oxidative balance in the liver over time, despite previous indications of oxidative stress in fetal livers affected by IUGR.

In our study, we observed intriguing changes in hepatocyte physiology reflected in serum levels of key enzymes such as IDH and MDH, tissue levels of GDH, G-6-PD, IDH, fumarase, and minerals such as zinc, and copper. Notably, while the levels of GDH, G6PD, and NADP-IDH normalized in the 8-week-old IUGR group, there were distinct alterations in serum and tissue levels of some other enzymes and minerals. For instance, serum IDH and MDH levels decreased whereas tissue NAD-IDH, fumarase, zinc, and copper levels were increased. Some of these enzymes play crucial roles in the citric acid cycle, a series of biochemical reactions essential for energy release through the oxidation of acetyl-CoA. Previous research has linked IUGR with compromised mitochondrial function, characterized by reduced ATP content, diminished complex activity, and downregulated expression of genes related to mitochondrial biogenesis and energy metabolism (Cheng *et al.,* 2021). Interestingly, our findings in the 8-week-old IUGR group revealed a complex interplay: while serum levels of IDH and MDH levels, principal enzymes of the citric acid cycle, decreased, tissue levels of NAD-IDH, and fumarase, indicative of mitochondrial energy metabolism, increased. This observation is pivotal as energy homeostasis controls tissue growth, with substrate utilization and oxidative phosphorylation playing crucial roles (Krebs 1970; Seppet *et al.,* 2009). Moreover, IUGR newborns often exhibit catch-up growth accompanied, as we detected in our study, by elevated resting energy expenditure (Chessex *et al.,* 1984; Davies *et al.,* 1996) potentially leading to overstimulation of the energy production cycle and the generation of excessive free radicals. The elevated liver copper levels observed in the 8-week-old IUGR group may also be linked to increased mitochondrial metabolism. For the assembly of cuproenzymes like the cytochrome-c oxidase and the antioxidant enzymes, mitochondria collect copper. Copper is essential for mitochondrial dynamics, aiding in energy metabolism, detoxification of reactive oxygen species, and signaling in eukaryotic organisms. Since copper homeostasis is tightly regulated by the liver (Ruiz *et al.,* 2021), significant alterations in copper levels may signify disturbances in liver metabolism. On the other hand, zinc facilitates mitochondrial pyruvate transport, oxidative phosphorylation, and regulation of energy metabolism. In conditions of toxin-induced stress, zinc plays a role in restoring energetic metabolism (Yang *et al.,* 2017). The observed elevation in zinc levels could potentially be a compensatory mechanism to regulate impaired energy metabolism. These findings underscore the intricate interplay between mitochondrial function, energy metabolism, and trace element homeostasis in the context of IUGR, shedding light on potential avenues for further investigation into liver metabolism and its implications for overall health.

In our study, we conducted an extensive analysis of metabolite levels using NMR spectroscopy analysis, aiming to identify potential disease associations linked to these alterations. We observed significant changes in various metabolites within the IUGR groups across different age groups. In the 2-week-old IUGR group, we noted increases in succinate, acetoacetate, isoleucine, cytidine, and formate levels while decreases in citrate, glucose, glucose-1-phosphate, maltose, isocitrate, and homocysteine levels. Interestingly, while most metabolites normalized in the 4-week-old IUGR group, some, like ethanol, pyruvate, cadaverine, and ethanolamine exhibited increased levels. Furthermore, in the 8-week- old IUGR group, acetoacetate levels remained elevated, alongside isoleucine, cytidine, and pyruvate levels were increased. Additionally, exclusive increases were observed in metabolites such as niacinamide, valine, phenylalanine, glutamate, cytidine, glucose, uracil, cadaverine, isoleucine, 1- methyhistidine, methionine, glucuronate, glycine, and fumarate. Overall, acetoacetate, isoleucine, succinate, valine, niacinamide, formate, pyruvate and cadaverine showed notable increases, while serine, nicotinurate, maltose, homocysteine, and citrate levels were decreased in the IUGR group compared to the Sham group. These changes can be indicative of various metabolic and pathological

conditions. For example, in both type I and II diabetes, cells may switch to alternative energy sources such as fatty acids, leading to increased ketogenesis and elevated tissue acetoacetate levels (She *et al.,* 2007). The persistent negative effects of IUGR on liver metabolism were evident even in later postnatal stages, despite IUGR puppies achieving growth levels comparable to healthy puppies shortly after birth. Metabolic pathways such as ketone body, butyrate, methionine, galactose, betaine, glycerol metabolisms, valine, leucine, and isoleucine degradation, were significantly induced by IUGR. These pathways remained affected even in the 8th postnatal week, indicating long-term metabolic alterations associated with IUGR. In contrast to a recent study by Gao *et al.,*2022), our findings differed in terms of enriched metabolic pathways. According to their study, linoleic acid and galactose metabolism, oxytocin signaling pathway, aldosterone synthesis, and unsaturated fatty acid biosynthesis were significantly enriched. Conversely, the levels of gamma-linolenic acid, arachidonic acid, hydroxy octadecanoic acids, and N-acetyl-D-galactosamine were significantly decreased in the IUGR groups. In our study valine, leucine and isoleucine degradation, ketone body, and butyrate metabolism were among the most affected metabolisms in the whole period and also among the most affected metabolisms according to the persistent abnormalities in the 8-week-old IUGR group. However, alterations in galactose metabolism and fatty acid biosynthesis were consistent between these two studies. Branched-chain amino acids (BCAAs), including valine, leucine, and isoleucine, play essential roles in stress response, energy production, protein synthesis, and overall metabolic health. Dysregulation of BCAAs has been linked to various metabolic diseases, such as insulin resistance (IR), obesity, heart failure, and cancer (Du *et al.,* 2022). The liver, known for its high metabolic efficiency, is crucial in the oxidative decarboxylation of branched-chain keto acids (BCKAs) (Shin *et al.,* 2014), highlighting its significance in metabolic regulation and disease pathogenesis. Elevated concentrations of plasma BCAAs, BCKAs, and carnitine esters have been reported in conditions like IR, obesity, and type-2 diabetes in patients and mice (She *et al.,* 2007).

Accumulation of BCKAs is also associated with glucose intolerance and cardiac insufficiency (East *et al.,* 2021), further underscoring the clinical relevance of BCCA metabolism. Additionally, the ketone bodies (KBs), such as β-hydroxybutyrate, and acetoacetate serve as important alternative energy sources during fasting. Increased levels of acetoacetate, a prominent metabolite observed in our study, suggest alterations in hepatic ketogenesis and metabolic reprogramming. Besides, the increase in hydroxybutyrate levels observed in our study further highlights the dysregulation of ketone body metabolism associated with IUGR. KBs, including acetoacetate and hydroxybutyrate, are synthesized through hepatic ketogenesis and serve as crucial alternative energy sources during periods of fasting or low glucose availability. KBs synthesized by hepatic ketogenesis are converted into acetyl- CoA in extrahepatic tissues, which then enter the citric acid cycle and are oxidized for energy (Hwang *et al.,* 2022). To enter the citric acid cycle, acetyl CoA first condenses with oxaloacetate derived from pyruvate during glycolysis. During periods of low glucose availability, such as fasting or in conditions like diabetes, oxaloacetate, a key intermediate in the citric acid cycle, is preferentially utilized for gluconeogenesis rather than condensing with acetyl-CoA to enter the citric acid cycle (Laffel 1999). As a result, acetyl-CoA is diverted towards KB formation, leading to increased production of KBs. Hepatic ketogenesis interfaces with other metabolic pathways, including fatty acid β-oxidation, the citric acid cycle, and gluconeogenesis (Cotter *et al.,* 2013) reflecting its integral role in metabolic hemostasis. Dysregulations in ketone body metabolism have been implicated in various disease states, including diabetes and heart failure (Hall *et al.,* 1984; Lommi *et al.,* 1997). In these conditions, alterations in KB levels and metabolism contribute to derangements and further exacerbate disease progression.

The findings from our study revealed significant alterations in phenylalanine and tyrosine metabolism, particularly in the 8-week-old IUGR group, suggesting a dysregulation in these pathways associated with IUGR. Galactose, glycerol, and betaine metabolism were among the most affected pathways in the whole postnatal period. Phenylalanine and tyrosine metabolism are closely interconnected, with phenylalanine being metabolized into acetoacetic acid and fumaric acid via tyrosine. Previous research by Tang *et al.,*Tang *et al.,* 2022) has also reported upregulated phenylalanine and tyrosine metabolisms in the IUGR piglet groups corroborating our findings. Additionally, Faverzani *et al.,*2021) highlighted the potentially detrimental effects of elevated phenylalanine levels and its keto acid derivatives, including DNA oxidative damage in glial cells. Accumulation of phenylalanine and its organic acid derivatives in tissues and biological fluids has been implicated in various adverse outcomes, including mental retardation (Casey 2013). Furthermore, our study and the metabolomics study of Gao *et al.* (2022) both identified galactose metabolism as one of the most affected pathways in the IUGR. Galactosemia, a disorder characterized by impaired galactose metabolism, has been associated with liver and kidney diseases, brain damage, and cataracts (Qi *et al.,* 2019).

Conclusion

Our study sheds light on the comprehensive metabolic alterations associated with IUGR in rats. The pups affected by IUGR were involved in a variety of changes including histological features, apoptosis rate, mitochondrial energy metabolism, propanoate metabolism, ketone body metabolism, butyrate metabolism, phenylalanine and tyrosine metabolism, valine, leucine, and isoleucine degradation. Importantly, our findings indicate that despite reaching similar levels of body development as normal-born offspring, rats with IUGR continue to experience ongoing dysregulation in several metabolic pathways. This suggests that the consequences of IUGR extend beyond early postnatal life and may predispose individuals to a range of health issues later in life. Furthermore, our metabolomics analysis provides insights into the potential disease susceptibility of individuals born with IUGR, including obesity, diabetes, heart failure, cancer, mental retardation, kidney and liver diseases, and cataracts. The identification of these metabolic changes underscores the importance of monitoring and managing the long-term health outcomes of individuals affected by IUGR. Overall, our study contributes to a deeper understanding of the hepatic metabolic characteristics associated with IUGR, providing a valuable theoretical framework for further research aimed at elucidating the underlying mechanisms and developing targeted interventions to mitigate the adverse effects of IUGR on long-term health.

Material and Methods

Experimental protocol

Fifty-four male siblings procured from 20 Sprague-Dawley female 4-month- old rats were used. The sample size for each group was determined via Power Analysis, ensuring 80% power and 95% confidence interval, with a maximum difference of 0.9 and a standard deviation of 0.9. For mating one male per two female rats per one cage were kept together overnight. The day of vaginal plaque detection was considered the 0.5th day of pregnancy. On the 19th day of gestation, half of the female rats underwent bilateral uterine artery ligation (IUGR group) while the other half underwent a simulated surgical intervention involving solely cutting and closure of the peritoneum (Sham group). All pregnant rats received standard care until natural delivery, thereafter, weaning their pups. The pups from the Sham and IUGR groups were euthanized under 50 mg/kg ketamine hydrochloride and 10 mg/kg 2% xylazine hydrochloride anesthesia at postnatal 2nd, 4th, and 8th weeks, and blood and liver samples were obtained. Blood samples for biochemical analysis were obtained via cardiac puncture. Half of the liver samples were stored at -80°C for metabolomics, biochemical, and Western blotting analysis, and the remaining tissues underwent preservation in 10% neutral buffered formaldehyde for histological examination.

All animal research conducted adhered to the guidelines in the Guide for the Care and Use of Laboratory Animals (8th edition, National Academies Press). Approval for the study was obtained from Bezmialem Vakıf University Local Ethics Committee for Animal Experiments. Furthermore, the project received support from the Scientific Research Unit of Bezmialem Vakif University (Project no: 20220411). These measures ensure the ethical treatment of animals and uphold the principles of responsible scientific inquiry.

Body weights of the pups

Body weights of the pups were measured just before the euthanasia process at the 2nd, 4^{th,} and 8th weeks.

Histopathological analyses

Following fixation, tissues underwent dehydration with alcohol and clearance with xylene before being embedded in paraffin. Subsequently, 5-µm sections were prepared and stained with hematoxylin-eosin (H&E) for microscopic evaluation. The number of central veins and portal areas were quantified in 6 microscope fields under 10X magnification. For immunohistochemical analysis, antibodies against caspase-8 (1:100 dilution, catalog no: ab25901, Abcam; UK) and Ki-67 (1:100 dilution, catalog no: PA5-19462, Merck; USA) were employed to detect apoptotic cells, proliferating cells, respectively. For this reason, the sections were placed in a 3% hydrogen peroxide solution for 20 minutes after the deparaffinization process. Following two rounds of 5 minutes in water, the pieces were microwave-mounted in a citrate solution for a duration of 20 minutes. The pieces were cleaned in water twice for 5 minutes each after cooling. Blocking solution was dropped on the sections and waited for 10 minutes. Subsequently, the sections were coated with the primary antibody and left overnight at +4°C. The samples were cleaned in water three times for 5 minutes the next day. After dropping the secondary antibody onto the sections, an hour was passed. Then the sections underwent three 5-minute rinses in water and dropped by a horseradish peroxidase (HRP) solution. Following another wash, the sections were coated with DAP chromogen, allowed to color, and examined under a light microscope. Finally, the sections were counterstained by Mayer's Hematoxylin about 2 minutes and following dehydration were covered with the coverslips. By the way, for validation of the specificities of the primary antibodies, the procedure described above was carried out using antibody diluent solution instead of primary antibody. Fifteen successive areas within each section were examined for immunopositivity at 40X magnification. Positive stained cells were counted in 15 successive frames which each had area of 33.900 µm^2 of hepatic parenchyma. All the analysis and imaging procedures were conducted using Nikon Eclipse i5 light microscope and Nikon NIS Elements version 4.0 imaging and analysis system (Nikon Instruments Inc., Tokyo, Japan).

Western-blotting analyses

After rinsing 0.1 M phosphate-buffered saline (PBS), liver tissues obtained from each animal was homogenized with PBS containing protease inhibitor cocktail (catalog no: 5872 Cell Signaling, Danvers, USA), with help of metallic beads. Homogenized tissues were centrifuged at

12.000 x *g* for 15 min at 4°C. The collected supernatants were used for sodium dodecyl sulfate- polyacrylamide gel electrophoresis (SDS-PAGE). Equal amounts of protein (40 µg/µL) which were determined with Pierce BCA Protein Assay Kit (Thermo Fisher Scientific, Waltham) by Multiskan™ GO Microplate Spectrophotometer were diluted in Laemmle sample buffer (Bio-Rad Laboratories, Inc. U.S.A), boiled for denaturation of proteins and loaded onto 4-20% Bis-Tris polyacrylamide gels and transferred into PVDF membranes using Bio-Rad protein electrophoresis and blotting system. Membranes were incubated in blocking solution (5% milk powder in 0.1% Tween 20/0.1 M Tris- buffered saline (TBST) and immersed with primary antibodies including RIP3 (1:1000 dilution (0,1 µg/mL), catalog no: ab152130, Abcam, Boston, USA) and NF-kβ (1:1000 dilution (0,208 µg/mL), catalog no: 8242, Cell Signaling, Danvers, USA). Each antibody was diluted in 5% milk powder in 0.1% Tween 20/0.1 M TBST in a 1:1000 dilution and incubated with the membrane by shaking overnight. The following day, membranes were rinsed and incubated in peroxidase-coupled secondary antibodies (anti- rabbit IgG, 1:5000 dilution (0,0154 µg/mL), catalog no: 7074, Cell Signaling, Danvers, USA) which were diluted in the same solvent as the primary antibodies. Signal detection was made with luminol substrate (Advansta, San Francisco, USA) under a CCD camera with Fusion FX7 system (Vilber Lourmat). Protein loading was controlled with a monoclonal mouse antibody against GAPDH (1: 1000, dilution (0,042 µg/mL), catalog no: 2118, Cell Signaling, Danvers, USA). Immunoreactive protein bands were quantified using the ImageJ analysis system (NIH; Washington, USA).

Biochemical analyses

Biochemical parameters encompassed Krebs cycle enzyme activities, specifically isocitrate dehydrogenase (IDH), glutamate dehydrogenase (GDH), malate dehydrogenase (MDH), and citrate synthase (CC). Additionally, trace elements such as copper (Cu) and zinc (Zn) were included, as well as markers associated with oxidative stress, namely total oxidant status (TOS), total antioxi-

dant status (TAS), total thiol (TThiol) and native thiol (NThiol) levels, and catalase enzyme activity. Serum levels of IDH, MDH, and GDH enzyme activity were evaluated using commercially available kits (RL 0949, RL 0925, RL 0932 Rel Assay Diagnostics, Gaziantep, Turkey) and automatic photometric methods performed by the Abbott ARCHITECT c8000 clinical chemistry analyzer. Serum and tissue TOS and TAS levels were determined using a fully automated colorimetric method developed by Ozturk *et al.,*Ozturk 2011). The oxidative stress index (OSI) was determined using the following formula: OSI (arbitrary unit) = TOS (μmol H2O2 Eq/L) divided by 10 times the TAS (mmol Trolox Eq/L). Serum levels of TThiol and NThiol were assessed using a novel method developed by Erel *et al.,*Erel *et al.,* 2020). Zinc concentrations (μg/dL) were quantified using the commercially available Rel Assay zinc measurement kit (Gaziantep, Turkey) with the aid of a fully automated photometric method executed on the Abbott ARCHITECT c8000 clinical chemistry analyzer. Copper concentrations (μg/dL) were measured employing the commercially available Rel Assay copper measurement kit (Gaziantep, Turkey), utilizing a fully automated photometric method on the Abbott ARCHITECT c8000 clinical chemistry analyzer.

NMR Spectroscopy analyses

NMR spectroscopy analyses were performed on both serum and hepatic tissue samples as follows.

NMR Spectroscopy analyses of serum samples

Blood samples previously collected and stored at -80°C were divided into two portions, one part allocated for biochemical analysis and the other part for metabolomics analysis. Previously reported NMR spectroscopy method was used to analyze serum samples, with slight modifications (Nagana Gowda *et al.,* 2014). According to that method, upon thawing at room temperature, 1 mL volume of each sample was combined with 2 mL cold methanol to induce precipitation of proteins. After 20 seconds of vortexing, the mixture was centrifuged at 10.000 x at 4°C for 1.5 hours and the supernatants of each sample were transferred to separate Eppendorf pipettes. Then supernatants were dried in a vacuum concentrator (Eppendorf™ Concentrator Plus) in V-AL mode at 60°C. Thus, methanol and water were completely removed from the mixture and the precipitated metabolites were allowed to accumulate at the bottom of the Eppendorf tubes. Later, each precipitate was dissolved in 500 μL of phosphate buffer (pH= 7.2, 60 mM), then 100 μL of deuterium oxide (D_2O) was added to each sample. Finally, 100 μL solution containing 1.75 mM trimethylsilyl propane sulfonic acid (DSS) was added to make the last concentration of 250 μM. A total of 700 μl of the final mixture was transferred to 5mm NMR tubes (Medium Wall Precision NMR Sample Tube, Wilmad) for subsequent NMR analyses. The NMR study was conducted using a 500 MHz Bruker Avance (Germany, Karlsruhe) located at the ILMER center of Bezmialem Vakif University. The 1D NOESY method was employed with the following parameters: acquisition time of 4 s, spectral width of 12 ppm, time domain of 2 s, delay time of 5 s, mixing time of 0.2 s, dummy scans of 8, scan number of 128, center of the spectrum at 4.7 ppm, and receiver gain set to 101. After completing the 1D NMR analyses, 10 μL of each sample was used to prepare quality control (QC) samples for each group. QC samples were analyzed using a 700 MHz Bruker Neo NMR spectrometer (Germany, Karlsruhe) with cryogenic probe capabilities, located at Gebze TUBITAK MAM in Turkey. Then 2D heteronuclear 1H-13C Heteronuclear Single Quantum Coherence (HSQC) Spectroscopy and homonuclear proton Total Correlation Spectroscopy (TOCSY) were conducted. The 1H-13C HSQC experiments were employed to obtain chemical shift correlations for protons directly attached to carbon atoms. TOCSY facilitated the generation of correlations between all protons within a given spin system, including non-geminal or non-vicinal protons. The HSQC Spectroscopy and TOCSY were acquired for each sample using the "hsqcetgpsisp2.2" and "dipsi2gpphzs" pulse sequences from Bruker's standard pulse catalog. The experiments were conducted on a 700 MHz NMR system equipped with a cryogenically cooled probe head (QCI CryoProbe) at 22 ºC. The spectral width for the 1H (F2) and 13C (F1) dimensions in HSQC Spectroscopy was set to 11.7 and 185 ppm, respectively, while the spectral width for TOCSY was set to 11.7 and 12.0 ppm, respectively. A total of 256 increments were recorded for each spectrum. The HSQC Spectroscopy consisted of 64 scans with a relaxation delay of 1.5 s per scan, while the TOCSY comprised 48 scans with a relaxation delay of 2 s. The mixing time for spin systems in all TOCSY was set to 80 ms. During spectral processing, a QSINC window function was applied to all Free Induction Decays (FIDs), and the linear prediction procedure was employed with a coefficient of 60 for HSQC spectroscopy and 48 for TOCSY.

NMR Spectroscopy analyses of tissue samples

Tissue samples stored at -80°C were thawed gradually to room temperature. The samples were weighed 100 mg/mL and homogenized utilizing a 60 mM phosphate buffer solution at a pH of 7.4. The homogenization process involved the use of beads to facilitate the extraction of hydrophilic metabolites (Zukunft *et al.,* 2018). Before filtration, the homogenized tissue supernatant underwent a centrifugation step at 1000 g for 20 minutes. Subsequently, the supernatant was filtered using a 40 μm cellulose acetate filter. Homogenate samples were divided into three distinct groups for metabolomics, biochemical, and Western blotting analysis. For NMR spectroscopy method 300 μl of tissue homogenates, 300 μL of phosphate buffer (pH= 7.4, 60 mM), and 100 μL of 1.75 mM trimethylsilyl propane sulfonic acid (DSS) in pure deuterium oxide (D_2O) was added to each sample with the last concentration of 250 μM. The entire 700 μL solution was transferred into 5 mm NMR tubes (Medium Wall Precision NMR Sample Tube, Wilmad) for subsequent analysis. The 1D and 2D NMR spectra were recorded using the same methods described for the serum samples above.

Metabolomics analyses

NMR Spectral process is performed as follows: The duration of 2D- dimensional NMR analysis for each sample was an average of 8-12 hours. Therefore, 2D NMR analyses were performed at least twice only on QC samples. The 2D HSQC and TOCSY spectra were processed using TopSpin software (v.4.1.3) with the following steps: zero-filling, Fourier transformation, phase correction, baseline correction, and peak alignment. For metabolite identification, the spectra were then converted to TopSpin ASCII format (.txt) and uploaded to the 'COLMARm 13C-1H HSQC, HSQC- TOCSY, and TOCSY Query and Verifica-

tion' program (https://spin.ccic.osu.edu/index.php/colmarm). Subsequently, identified metabolites were included in the Chenomx NMR suite V10.1 program (Chenomx, Inc., Edmonton, AB, Canada) for quantitation in the 1D NOESY spectrum. The quantification was based on the results of 1D NOESY experiments, where specific proton signals corresponding to compounds and the internal standard DSS were manually integrated. Phase correction, line broadening (0.3 Hz) and zero-filling factors were automatically adjusted. The chemical shift values of the analytes were calibrated using DSS (0.0 ppm). The relative concentrations of the metabolites were calculated using the 1H NMR spectrum signal intensity method, with DSS serving as the internal standard.

Statistical and chemometric analysis

The descriptive statistics for the quantitative variables in the study were provided as mean, median, standard deviation, minimum, and maximum. The normality of the quantitative variables was assessed using the Shapiro-Wilk test. The homogeneity of variances was assessed using the Levene test. Student's t-test was used for comparing the means of two independent groups, while the Mann-Whitney U test was used for comparing the medians of two independent groups. ANOVA was employed for comparing means of more than two independent groups, and for *post hoc* multiple comparisons, the Tukey LSD test was used. Relationships between quantitative variables were evaluated using Spearman correlation analysis. A statistical significance level of 0.05 was adopted, and calculations were performed using the SPSS (version 26) software package.

Spearman correlation analysis was conducted with the means of metabolites. The identified metabolite list obtained through NMR analysis and biochemical analysis was transferred to MetabolAnalyst 5.0 software for data reduction and visualization. A meta-analysis method was employed in this study, which involved the utilization of p-values obtained from various datasets. These p-values were combined using Stouffer's method. Before conducting the chemometric analysis, the data underwent a preprocessing step that involved sample normalization using either the sum or median method. Additionally, data normalization techniques such as logarithm base 10 transformation, square root transformation, or cube root transformation were applied. For data scaling, methods such as mean centering or auto-scaling were employed. The metabolites that displayed the most significant differentiation between groups were subjected to individual testing using the exact Wilcoxon rank-sum test to determine the significance of differences in their levels. The statistically significant differential metabolites were visualized by the generation of a Volcano Plot with large magnitude fold-changes (x- axis) and high statistical significance (-log10 of p-value, y-axis). Linear discriminant models were constructed utilizing quantified ratios of metabolites as input features. On concentration-based data, visualization was conducted using both unsupervised analysis methods: Partial Least Squares Regression Analysis and Orthogonal Partial Least Squares Projection to Latent Structures Discriminant Analysis (OPLS-DA) followed by obtaining Variable Importance Plots (VIP). The metabolite set enrichment (MSEA) and pathway impact analyses were done with MetaboAnalyst 5.0 to assess a set of metabolites that are biologically meaningful for certain pathways.

References

BARKER D. J. P. (2007). The origins of the developmental origins theory. *Journal of Internal Medicine* 261: 412-417. https://doi.org/10.1111/j.1365-2796.2007.01809.x

CASEY L. (2013). Caring for children with phenylketonuria. *Canadian family physician Medecin de famille canadien* 59: 837-840. CHENG K., JIA P., JI S., SONG Z., ZHANG H., ZHANG L., WANG T. (2021). Improvement of the hepatic lipid status in intrauterine growth retarded pigs by resveratrol is related to the inhibition of mitochondrial dysfunction, oxidative stress and inflammation. *Food & Function* 12: 278-290. https://doi.org/10.1039/D0FO01459A

CHESSEX P., REICHMAN B., VERELLEN G., PUTET G., SMITH J. M., HEIM T., SWYER P. R. (1984). Metabolic Consequences of Intrauterine Growth Retardation in Very Low Birthweight Infants. *Pediatric Research* 18: 709-713. https://doi.org/10.1203/00006450-198408000-00006

CIANFARANI S., AGOSTONI C., BEDOGNI G., BERNI CANANI R., BRAMBILLA P., NOBILI V., PIETROBELLI A. (2012). Effect of intrauterine growth retardation on liver and long-term metabolic risk. *International Journal of Obesity* 36: 1270-1277. https://doi.org/10.1038/ijo.2012.54

COTTER D. G., SCHUGAR R. C., CRAWFORD P. A. (2013). Ketone body metabolism and cardiovascular disease. *American Journal of Physiology-Heart and Circulatory Physiology* 304: H1060-H1076. https://doi.org/10.1152/ajpheart.00646.2012

DAVIES P. S., CLOUGH H., BISHOP N. J., LUCAS A., COLE J. J., COLE T. J. (1996). Total energy expenditure in small for gestational age infants. *Archives of Disease in Childhood - Fetal and Neonatal Edition* 75: F46-F48. https://doi.org/10.1136/fn.75.1.F46

DESSÌ A., ATZORI L., NOTO A., ADRIAAN VISSER G. H., GAZZOLO D., ZANARDO V., BARBERINI L., PUDDU M., OTTONELLO G., ATZEI A., MAGISTRIS A. D., LUSSU M., *et al.* (2011). Metabolomics in newborns with intrauterine growth retardation (IUGR): urine reveals markers of metabolic syndrome. *The Journal of Maternal-Fetal & Neonatal Medicine* 24: 35-39. https://doi.org/10.3109/14767058.2011.605868

DU C., LIU W.J., YANG J., ZHAO S.S., LIU H.X. (2022). The Role of Branched-Chain Amino Acids and Branched-Chain α-Keto Acid Dehydrogenase Kinase in Metabolic Disorders. *Frontiers in Nutrition* 9: 932670. https://doi.org/10.3389/fnut.2022.932670

EAST M. P., LAITINEN T., ASQUITH C. R. M. (2021). BCKDK: an emerging kinase target for metabolic diseases and cancer. *Nature Reviews Drug Discovery* 20: 498-498. https://doi.org/10.1038/d41573-021-00107-6

EREL Ö., ERDOĞAN S. (2020). Thiol-disulfide homeostasis: an integrated approach with biochemical and clinical aspects. *Turkish journal of medical sciences* 50: 1728-1738. https://doi.org/10.3906/sag-2003-64

FAVERZANI J. L., STEINMETZ A., DEON M., MARCHETTI D. P., GUERREIRO G., SITTA A., DE MOURA COELHO D., LOPES F. F., NASCIMENTO L. V. M., STEFFENS L., HENN J. G., FERRO M. B., *et al.* (2021). L-carnitine protects DNA oxidative damage induced by phenylalanine and its keto acid derivatives in neural cells: a possible pathomechanism and adjuvant therapy for brain injury in phenylketonuria. *Metabolic Brain Disease* 36: 1957-1968. https://doi.org/10.1007/s11011-021-00780-x

FOWDEN A. L., GIUSSANI D. A., FORHEAD A. J. (2006). Intrauterine Programming of Physiological Systems: Causes and Consequences. *Physiology* 21: 29-37. https://doi.org/10.1152/physiol.00050.2005

GAO H., CHEN X., ZHAO J., XUE Z., ZHANG L., ZHAO F., WANG B., WANG L. (2022). Integrative Analysis of Liver Metabolomics and Transcriptomics Reveals Oxidative Stress in Piglets with Intrauterine Growth Restriction. *Biology* 11: 1430. https://doi.org/10.3390/biology11101430

GODFREY K. M., GLUCKMAN P. D., HANSON M. A. (2010). Developmental origins of metabolic disease: life course and intergenerational perspectives. *Trends in Endocrinology & Metabolism* 21: 199-205. https://doi.org/10.1016/j.tem.2009.12.008

GURUGUBELLI KRISHNA R., VISHNU BHAT B. (2018). Molecular mechanisms of intrauterine growth restriction. *The Journal of Maternal-Fetal & Neonatal Medicine* 31: 2634-2640. https://doi.org/10.1080/14767058.2017.1347922

HALL S.E., WASTNEY M.E., BOLTON T.M., BRAATEN J.T., BERMAN M. (1984). Ketone body kinetics in humans: the effects of insulin-dependent diabetes, obesity, and starvation. *Journal of Lipid Research* 25: 1184-1194. https://doi.org/10.1016/S0022-2275(20)34462-X

HWANG C. Y., CHOE W., YOON K.S., HA J., KIM S. S., YEO E.J., KANG I. (2022). Molecular Mechanisms for Ketone Body Metabolism, Signaling Functions, and Therapeutic Potential in Cancer. *Nutrients* 14: 4932. https://doi.org/10.3390/nu14224932

KREBS H.A. (1970). Rate control of the tricarboxylic acid cycle. *Advances in Enzyme Regulation* 8: 335-353. https://doi.org/10.1016/0065-2571(70)90028-2

LAFFEL L. (1999). Ketone bodies: a review of physiology, pathophysiology and application of monitoring to diabetes. *Diabetes/Metabolism Research and Reviews* 15: 412-426. https://doi.org/10.1002/(SICI)1520-7560(199911/12)15:6<412::AID-DMRR72>3.0.CO;2-8

LANE R. H., FLOZAK A. S., OGATA E. S., BELL G. I., SIMMONS R. A. (1996). Altered Hepatic Gene Expression of Enzymes Involved in Energy Metabolism in the Growth-Retarded Fetal Rat. *Pediatric Research* 39: 390-394. https://doi.org/10.1203/00006450-199603000-00003

LIU J., WANG X.F., WANG Y., WANG H.W., LIU Y. (2014). The Incidence Rate, High-Risk Factors, and Short- and Long-Term Adverse Outcomes of Fetal Growth Restriction. *Medicine* 93: e210. https://doi.org/10.1097/MD.0000000000000210

LIU Y., AZAD M. A. K., ZHANG W., XIONG L., BLACHIER F., YU Z., KONG X. (2022). Intrauterine growth retardation affects liver bile acid metabolism in growing pigs: effects associated with the changes of colonic bile acid derivatives. *Journal of Animal Science and Biotechnology* 13: 117. https://doi.org/10.1186/s40104-022-00772-6

LOMMI J., KOSKINEN P., NÄVERI H., HÄRKÖNEN M., KUPARI M. (1997). Heart failure ketosis. *Journal of Internal Medicine* 242: 231-238. https://doi.org/10.1046/j.1365-2796.1997.00187.x

NAGANA GOWDA G. A., RAFTERY D. (2014). Quantitating Metabolites in Protein Precipitated Serum Using NMR Spectroscopy. *Analytical Chemistry* 86: 5433-5440. https://doi.org/10.1021/ac5005103

OGATA E. S., BUSSEY M. E., FINLEY S. (1986). Altered gas exchange, limited glucose and branched chain amino acids, and hypoinsulinism retard fetal growth in the rat. *Metabolism* 35: 970-977. https://doi.org/10.1016/0026-0495(86)90064-8

OGATA E. S., SWANSON S. L., COLLINS J. W., FINLEY S. L. (1990). Intrauterine Growth Retardation: Altered Hepatic Energy and Redox States in the Fetal Rat. *Pediatric Research* 27: 56-63. https://doi.org/10.1203/00006450-199001000-00017

OKE S. L., HARDY D. B. (2021). The Role of Cellular Stress in Intrauterine Growth Restriction and Postnatal Dysmetabolism. *International Journal of Molecular Sciences* 22: 6986. https://doi.org/10.3390/ijms22136986

OZTURK E., BALAT O., ACILMIS Y. G., OZCAN C., PENCE S., EREL Ö. (2011). Measurement of the placental total antioxidant status in preeclamptic women using a novel automated method. *Journal of Obstetrics and Gynaecology Research* 37: 337-342. https://doi.org/10.1111/j.1447-0756.2010.01346.x

PENDLETON A. L., WESOLOWSKI S. R., REGNAULT T. R. H., LYNCH R. M., LIMESAND S. W. (2021). Dimming the Powerhouse: Mitochondrial Dysfunction in the Liver and Skeletal Muscle of Intrauterine Growth Restricted Fetuses. *Frontiers in Endocrinology* 12: 612888. https://doi.org/10.3389/fendo.2021.612888

PONSUKSILI S., MURANI E., HADLICH F., IQBAL M. A., FUCHS B., GALUSKA C. E., PERDOMO-SABOGAL A., SARAIS F., TRAKOOLJUL N., REYER H., OSTER M., WIMMERS K. (2022). Prenatal transcript levels and metabolomics analyses reveal metabolic changes associated with intrauterine growth restriction and sex. *Open Biology* 12: 220151. https://doi.org/10.1098/rsob.220151

QI X., TESTER R. F. (2019). Fructose, galactose and glucose – In health and disease. *Clinical Nutrition ESPEN* 33: 18-28. https://doi.org/10.1016/j.clnesp.2019.07.004

RASHID C. S., BANSAL A., SIMMONS R. A. (2018). Oxidative Stress, Intrauterine Growth Restriction, and Developmental Programming of Type 2 Diabetes. *Physiology* 33: 348-359. https://doi.org/10.1152/physiol.00023.2018

RUIZ L. M., LIBEDINSKY A., ELORZA A. A. (2021). Role of Copper on Mitochondrial Function and Metabolism. *Frontiers in Molecular Biosciences* 8: 711227. https://doi.org/10.3389/fmolb.2021.711227

SAKER M., SOULIMANE MOKHTARI N., MERZOUK S. A., MERZOUK H., BELARBI B., NARCE M. (2008). Oxidant and antioxidant status in mothers and their newborns according to birthweight. *European Journal of Obstetrics & Gynecology and Reproductive Biology* 141: 95-99. https://doi.org/10.1016/j.ejogrb.2008.07.013

SEPPET E., GRUNO M., PEETSALU A., GIZATULLINA Z., NGUYEN H. P., VIELHABER S., WUSSLING M. H.P., TRUMBECKAITE S., ARANDARCIKAITE O., JERZEMBECK D., SONNABEND M., JEGOROV K., *et al.* (2009). Mitochondria and Energetic Depression in Cell Pathophysiology. *International Journal of Molecular Sciences* 10: 2252-2303. https://doi.org/10.3390/ijms10052252

SHARMA D., SHASTRI S., FARAHBAKHSH N., SHARMA P. (2016). Intrauterine growth restriction – part 1. *The Journal of Maternal-Fetal & Neonatal Medicine* 29: 3977-3987. https://doi.org/10.3109/14767058.2016.1152249

SHARMA D., SHARMA P., SHASTRI S. (2017). Genetic, metabolic and endocrine aspect of intrauterine growth restriction: an update. *The Journal of Maternal-Fetal & Neonatal Medicine* 30: 2263-2275. https://doi.org/10.1080/14767058.2016.1245285

SHE P., VAN HORN C., REID T., HUTSON S. M., COONEY R. N., LYNCH C. J. (2007). Obesity-related elevations in plasma leucine are associated with alterations in enzymes involved in branched-chain amino acid metabolism. *American Journal of Physiology-Endocrinology and Metabolism* 293: E1552-E1563. https://doi.org/10.1152/ajpendo.00134.2007

SHIN A. C., FASSHAUER M., FILATOVA N., GRUNDELL L. A., ZIELINSKI E., ZHOU J.Y., SCHERER T., LINDTNER C., WHITE P. J., LAPWORTH A. L., ILKAYEVA O., KNIPPSCHILD U., *et al.* (2014). Brain Insulin Lowers Circulating BCAA Levels by Inducing Hepatic BCAA Catabolism. *Cell Metabolism* 20: 898-909. https://doi.org/10.1016/j.cmet.2014.09.003

SIMMONS R. A., GOUNIS A. S., BANGALORE S. A., OGATA E. S. (1992). Intrauterine Growth Retardation: Fetal Glucose Transport is Diminished in Lung but Spared in Brain. *Pediatric Research* 31: 59-63. https://doi.org/10.1203/00006450-199201000-00011

SMITH C. V., HANSEN T. N., MARTIN N. E., MCMICKEN H. W., ELLIOTT S. J. (1993). Oxidant Stress Responses in Premature Infants during Exposure to Hyperoxia. *Pediatric Research* 34: 360-365. https://doi.org/10.1203/00006450-199309000-00024

SULLIVAN J. L., NEWTON R. B. (1988). Serum antioxidant activity in neonates. *Archives of Disease in Childhood* 63: 748-750. https://doi.org/10.1136/adc.63.7_Spec_No.748

TANG W., ZHANG W., AZAD M. A. K., MA C., ZHU Q., KONG X. (2022). Metabolome, microbiome, and gene expression alterations in the colon of newborn piglets with intrauterine growth restriction. *Frontiers in Microbiology* 13: 989060. https://doi.org/10.3389/fmicb.2022.989060

VUGUIN P. M. (2007). Animal Models for Small for Gestational Age and Fetal Programing of Adult Disease. *Hormone Research in Paediatrics* 68: 113-123. https://doi.org/10.1159/000100545

WANG J., CHEN L., LI D., YIN Y., WANG X., LI P., DANGOTT L. J., HU W., WU G. (2008). Intrauterine Growth Restriction Affects the Proteomes of the Small Intestine, Liver, and Skeletal Muscle in Newborn Pigs. *The Journal of Nutrition* 138: 60-66. https://doi.org/10.1093/jn/138.1.60

WANG J., ZHU P., ZHENG X., MA Z., CUI C., WU C., ZENG X., GUAN W., CHEN F. (2022). Altered Liver Metabolism, Mitochondrial Function, Oxidative Status, and Inflammatory Response in Intrauterine Growth Restriction Piglets with Different Growth Patterns before Weaning. *Metabolites* 12: 1053. https://doi.org/10.3390/metabo12111053

WIGGLESWORTH J. S. (1964). Experimental growth retardation in the foetal rat. *The Journal of Pathology and Bacteriology* 88: 1-13. https://doi.org/10.1002/path.1700880102

YANG X., WANG H., HUANG C., HE X., XU W., LUO Y., HUANG K. (2017). Zinc enhances the cellular energy supply to improve cell motility and restore impaired energetic metabolism in a toxic environment induced by OTA. *Scientific Reports* 7: 4669. https://doi.org/10.1038/s41598-017-14868-x

ZHANG H., SU W., YING Z., CHEN Y., ZHOU L., LI Y., ZHANG J., ZHANG L., WANG T. (2018). N-acetylcysteine attenuates intrauterine growth retardation-induced hepatic damage in suckling piglets by improving glutathione synthesis and cellular homeostasis. *European Journal of Nutrition* 57: 327-338. https://doi.org/10.1007/s00394-016-1322-x

ZHANG H., FAN Y., ELSABAGH M., GUO S., WANG M., JIANG H. (2020). Dietary Supplementation of L-Arginine and N-Carbamylglutamate Attenuated the Hepatic Inflammatory Response and Apoptosis in Suckling Lambs with Intrauterine Growth Retardation. *Mediators of Inflammation* 2020: 1-10. https://doi.org/10.1155/2020/2453537

ZHANG H., CHEN Y., CHEN Y., JI S., JIA P., XU J., LI Y., WANG T. (2021). Pterostilbene attenuates liver injury and oxidative stress in intrauterine growth–retarded weanling piglets. *Nutrition* 81: 110940. https://doi.org/10.1016/j.nut.2020.110940

ZUKUNFT S., PREHN C., RÖHRING C., MÖLLER G., HRABĚ DE ANGELIS M., ADAMSKI J., TOKARZ J. (2018). High-throughput extraction and quantification method for targeted metabolomics in murine tissues. *Metabolomics* 14: 18. https://doi.org/10.1007/s11306-017-1312-x